

AEDC-TR-75-154

12



ANALYSIS, DESIGN, AND TESTING OF COMPONENTS
OF A COMBINED ABLATION/EROSION NOZZLE

ADA021963

PROPELLION WIND TUNNEL FACILITY
ARNOLD ENGINEERING DEVELOPMENT CENTER
AIR FORCE SYSTEMS COMMAND
ARNOLD AIR FORCE STATION, TENNESSEE 37389

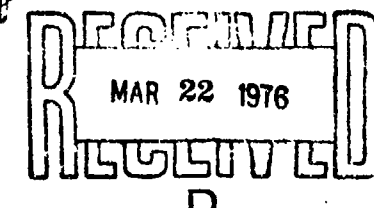
March 1976

Final Report for Period July 1, 1973 – June 30, 1975

Approved for public release; distribution unlimited.

Prepared for

DIRECTORATE OF TECHNOLOGY (DY)
ARNOLD ENGINEERING DEVELOPMENT CENTER
ARNOLD AIR FORCE STATION, TENNESSEE 37389



NOTICES

When U. S. Government drawings specifications, or other data are used for any purpose other than a definitely related Government procurement operation, the Government thereby incurs no responsibility nor any obligation whatsoever, and the fact that the Government may have formulated, furnished, or in any way supplied the said drawings, specifications, or other data, is not to be regarded by implication or otherwise, or in any manner licensing the holder or any other person or corporation, or conveying any rights or permission to manufacture, use, or sell any patented invention that may in any way be related thereto.

Qualified users may obtain copies of this report from the Defense Documentation Center.

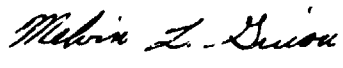
References to named commercial products in this report are not to be considered in any sense as an endorsement of the product by the United States Air Force or the Government.

This report has been reviewed by the Information Office (OI) and is releasable to the National Technical Information Service (NTIS). At NTIS, it will be available to the general public, including foreign nations.

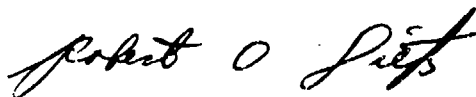
APPROVAL STATEMENT

This technical report has been reviewed and is approved for publication.

FOR THE COMMANDER



MELVIN L. GINSON
Captain, USAF
Research & Development
Division
Directorate of Technology



ROBERT O. DIETZ
Director of Technology

UNCLASSIFIED

DD FORM 1 JAN 73 1473 EDITION OF 1 NOV 65 IS OBSOLETE

UNCLASSIFIED
042550

UNCLASSIFIED

20. ABSTRACT (Continued)

to produce 4,000- to 5,000-ft/sec particle velocities in a flow having an impact pressure of 80 atm. A cold-flow version of this facility was designed, fabricated, and operated to provide initial experience with the new configuration.

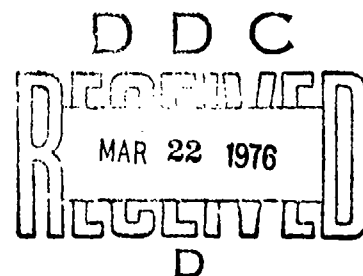
AMAC
Arnold AMAC Tenn

UNCLASSIFIED

PREFACE

The work reported herein was conducted by the Arnold Engineering Development Center (AEDC), Air Force Systems Command (AFSC), under Program Element 65807F. The results of the test were obtained by ARO, Inc. (a subsidiary of Sverdrup & Parcel and Associates, Inc.), contract operator of AEDC, AFSC, Arnold Air Force Station, Tennessee, under ARO Projects No. PF403, PF404, and P32S-22B. The authors of this report were K. P. Fewell and P. A. Kessel, ARO, Inc. The data analysis was completed on June 1, 1975, and the manuscript (ARO Control No. ARO-PWT-TR-75-107) was submitted for publication on June 30, 1975.

ACCESSION FOR	
NTIS	White Section <input checked="" type="checkbox"/>
DDC	Buff Section <input type="checkbox"/>
UNANNOUNCED	<input type="checkbox"/>
JUSTIFICATION	<input type="checkbox"/>
.....	
BY.....	
DISTRIBUTION/AVAILABILITY CODES	
Dist.	AVAIL. AND OR SPECIAL
A	



CONTENTS

	<u>Page</u>
1.0 INTRODUCTION	7
2.0 COMPUTER PROGRAMS FOR ANALYSIS OF GAS/PARTICLE FLOWS	
2.1 One-Dimensional Gas/Particle Flow with Thick Boundary Layers	10
2.2 Two-Dimensional Trajectory Calculations in Particle/Gas Flow	13
2.3 Particle Drag Coefficients	14
3.0 EXPERIMENTAL EVALUATION OF GAS/PARTICLE FLOW PROGRAMS	
3.1 Evaluation of the One-Dimensional Particle Acceleration Program.	18
3.2 Two-Dimensional Trajectory Experiment in the Dust Erosion Tunnel.	31
4.0 ANALYSIS AND DESIGN OF A COMBINED ABLATION/EROSION NOZZLE	
4.1 Parametric Design Study of Ablation/Erosion Nozzle.	37
4.2 Detail Design of a First-Generation Ablation/Erosion Nozzle.	40
5.0 DESIGN AND TESTING OF COLD-FLOW ABLATION/EROSION NOZZLE	
5.1 Design Considerations	43
5.2 Experimental Apparatus.	44
5.3 Experimental Results	46
6.0 CONCLUSIONS.	50
REFERENCES	51

ILLUSTRATIONS

Figure

1. Gas Velocity, Particle Velocity, and Temperature in an M = 2.0 Ablation Nozzle, D* = 0.375 in.	8
2. Proposed Ablation/Erosion Nozzle Concept	9
3. Sphere Drag Coefficient versus Reynolds Number	15
4. Comparison of Curve Fit and AEDC Data on Sphere Drag Coefficient.	17

<u>Figure</u>	<u>Page</u>
5. Photomicrographs of Particle Samples Showing Individual Shapes	18
6. Particle Size Histograms	
a. 100- μ MgO Particles and 100- μ Glass Beads	18
b. 1- μ TiO ₂ Particles	19
7. Gas Velocity, Mach Number, Particle Velocity, and Temperature in DET Nozzle, D* = 0.563 in.	
a. Throat Region	21
b. Supersonic Section	21
8. Comparison of Calculated and Measured Particle Velocities in DET	22
9. Gas Velocity, Particle Velocity, and Temperature in Helium Acceleration Nozzle, D* = 0.119 in.	23
10. Calculated Particle Acceleration in Light-Gas Particle Acceleration, Helium	23
11. Cross Section of Stilling Chamber and Nozzle of Light-Gas Accelerator	24
12. Photographs of Light-Gas Particle Accelerator Apparatus	
a. Heater End of Apparatus	26
b. Exit of Nozzle	26
13. Pitot Pressure and Mach Number Profiles in Light-Gas Particle Acceleration Nozzle Operated with Air	27
14. Mach Number and Calculated Particle Velocity in Light-Gas Accelerator, Air	28
15. Mach Number and Calculated Particle Velocity in Light-Gas Accelerator, Helium	29
16. Photographs of Impact Bars after 1-sec Exposure to 50- μ MgO Particles, Air and Helium	29
17. Photographs of Impact Bar after Exposure to 100- μ Glass Beads at 3,200 ft/sec (Calculated)	30

Figure	<u>Page</u>
18. Summary of Particle Velocity Measurements in DET and Light-Gas Particle Acceleration Nozzle, 100- μ MgO Particles	31
19. Schematic of AEDC/PWT Dust Erosion Tunnel (DET)	32
20. Photograph of Prandtl-Meyer Expansion Test Model	32
21. Photograph of Prandtl-Meyer Expansion Test Model after Run in DET	34
22. Photomicrograph of Impact Bar from Prandtl-Meyer Test Model	35
23. Trajectory Measurements for 25- μ Glass Beads in Prandtl-Meyer Expansion Test in DET	35
24. Summary of Particle Deflection Data 6.65 in. from Prandtl-Meyer Corner, DET, $M = 5$	36
25. Results of Flow-Field Calculations for Proposed Ablation/Erosion Nozzle	38
26. Particle Trajectories Calculated in Ablation/Erosion Nozzle	39
27. Cross Section of Ablation/Erosion Nozzle, Hot-Flow Version	42
28. Cross Section of Ablation/Erosion Nozzle, Cold-Flow Version	44
29. Photographs of Cold-Flow Ablation/Erosion Nozzle Apparatus	45
30. Shadowgraph of Flow in Cold-Flow Nozzle, No Skimmers	47
31. Shadowgraphs of Flow in Cold-Flow Nozzle, with Wedge Skimmer, Normal Wedge Position, and Adjusted Wedge Position	48

TABLES

1. Constants in Skin Friction Relation Eq. (5)	11
2. Interim Curve-Fit to Sphere Drag Coefficients	16

<u>Figure</u>	<u>Page</u>
3. Conditions for Prandtl-Meyer Flow Tests in Dust Erosion Tunnel	33
4. Characteristics of Trajectories in Ablation/ Erosion Nozzle	39
5. Design Conditions for First-Generation Ablation/Erosion Nozzle, Hot-Flow and Cold-Flow Versions	41
NOMENCLATURE	52

1.0 INTRODUCTION

In the past several years, the already imposing requirements of test facilities designed to evaluate the ablation response of materials have been further complicated by an emerging interest in erosion by hypervelocity particle impact. Such erosion of heat shield material is known to occur when a reentry vehicle traverses a cloud of solid or liquid particles at hypersonic speeds. These clouds may be of natural or man-made origin and contain particles with diameters up to $1,000 \mu$, although the range of primary interest is 50 to 500μ . Hypervelocity impact of a stream of particles on a solid surface can both increase the heat-transfer rate to the surface and remove base material by mechanical fracture of surface elements.

The basic physical processes involved in particle erosion can best be studied on a single impact basis in a ballistic range facility. In such a facility, the velocity, shape, and mass of the impacting body can be very accurately determined. The net erosion process, however, is composed of a great number of successive impacts occurring at a high rate on a given area of exposed surface. To study this process, test facilities have been developed which produce large numbers of impacts. Particle cloud generators have been developed for gun ranges. To produce erosion simulation for times longer than the flight time in a gun range, particle injection systems have been developed for use in wind tunnels. In the AEDC/PWT Dust Erosion Tunnel (DET), for example, solid particles of 50- to $500\text{-}\mu$ diameter are accelerated to velocities of 4,000 to 6,000 ft/sec. To attain these high velocities with particles of these diameters, it is necessary to drag-accelerate them in a long, unconventional nozzle having a very slow rate of expansion. However, even though it is an arc-heated facility, the DET does not qualify as an ablation facility because the heating rates produced in this unconventional nozzle are relatively low.

Since erosion and ablation often occur simultaneously in flight, there is considerable interest in developing a test facility having a combined capability. Although particle velocities of 18,000 ft/sec are encountered in flight, it is considered that velocities of 8,000 ft/sec or greater would be of interest in a ground test facility, with particle diameters of 50- to $500\text{-}\mu$. As an outgrowth of the RHEA facility feasibility studies at AEDC, a facility configuration for simultaneous ablation and erosion testing has been proposed, and this report describes the analytical and experimental investigations for evaluation of the new concept.

Calculation of the acceleration of particles injected directly into the nozzle of a conventional arc-heated ablation facility showed that because of the short length of the nozzle, final velocity of $100\text{-}\mu$ particles would be less than one-half the gas velocity (Fig. 1). The nozzles for typical ablation facilities are kept to a short length to minimize heat losses to the walls. High particle velocity and high heating rates appear to be mutually incompatible in arc-heater nozzles.

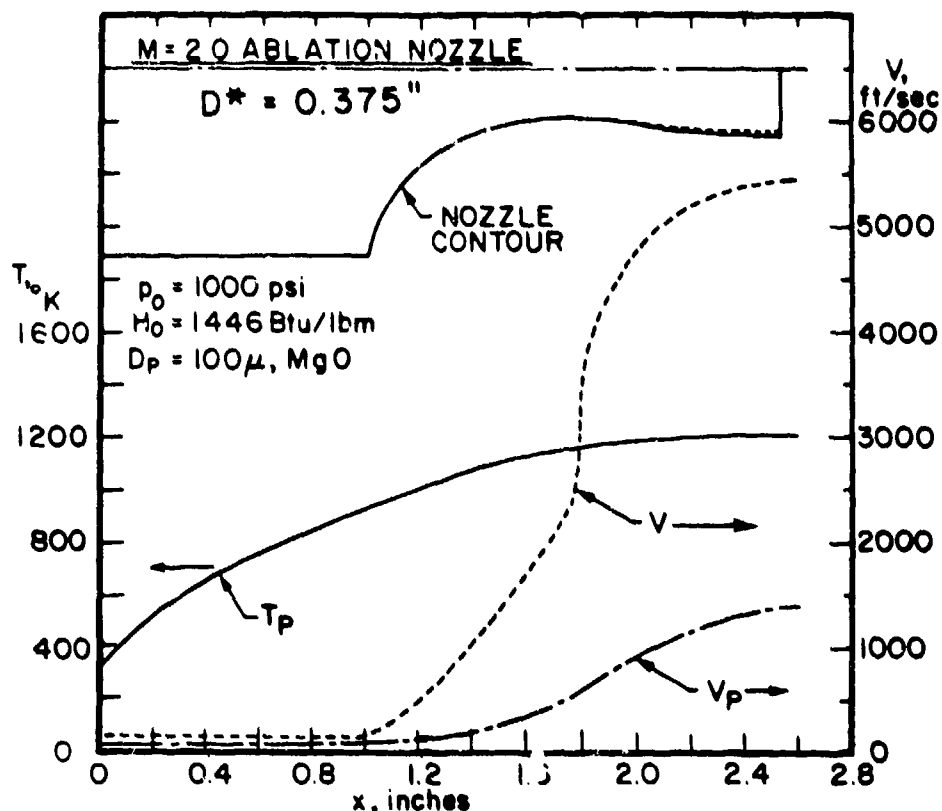


Figure 1. Gas velocity, particle velocity, and temperature in an $M = 2.0$ ablation nozzle, $D^* = 0.375$ in.

Studies of the RHEA facility (Ref. 1), an advanced concept involving dynamic interaction of particle and light-gas flows, focused attention on two phenomena which have since been incorporated into a proposed ablation/erosion facility. First, is the well-known capacity of a light gas to provide high gas velocities for relatively moderate stagnation temperatures. Second, as indicated by general particle trajectory studies, particles on the order of $100\text{-}\mu$ diameter traveling at thousands of feet per second are highly resistant to deflection caused

by aerodynamic forces imposed by most flow fields of interest. That is, the trajectories of such particles will be very nearly linear. A facility concept which utilizes these two phenomena is shown in Fig. 2.

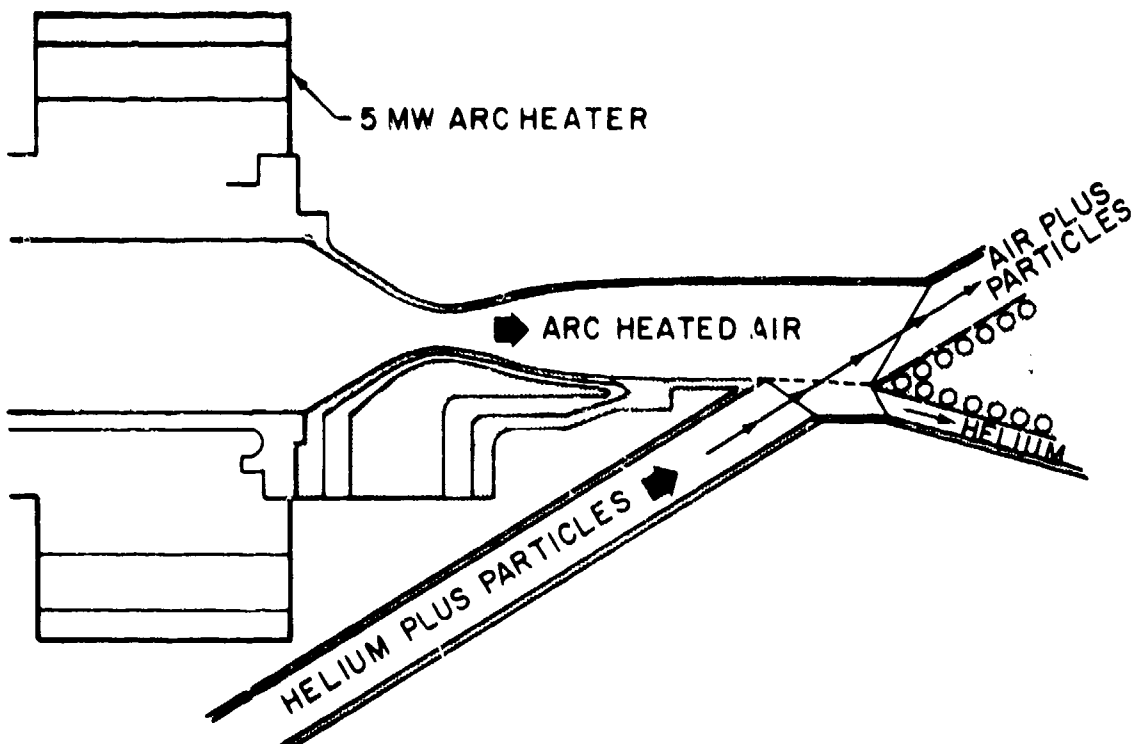


Figure 2. Proposed ablation/erosion nozzle concept.

In this proposed facility, ablation capability is obtained by use of a conventional high-pressure arc heater operating with air. Particles are accelerated to hypervelocities in a separate light-gas acceleration nozzle and then transferred to the ablation jet by impinging the two flows and allowing particle momentum to effect the transfer across the mixing layer. Analysis and several experimental efforts related to the feasibility of this concept are reported herein.

2.0 COMPUTER PROGRAMS FOR ANALYSIS OF GAS/PARTICLE FLOWS

Several computer programs were used in the analysis of a combined ablation/erosion nozzle. In each of these, the particle drag coefficient is an important parameter, and two different drag correlations were used.

2.1 ONE-DIMENSIONAL GAS/PARTICLE FLOW WITH THICK BOUNDARY LAYERS

The simplest conceptual approach to producing high speed in particles entrained in a gas is to inject the particles upstream of the throat of a supersonic nozzle and allow drag acceleration to the desired velocity level. A quasi-one-dimensional computer program was previously developed at AEDC/VKF for calculating such particle acceleration in supersonic nozzles having turbulent boundary layers on the nozzle wall (Ref. 2). This program was used to analyze the nozzle-particle flow shown in Fig. 1 for a conventional low Mach number nozzle and also to design the acceleration nozzle of the DET. In the latter case, it was found that optimization of a nozzle for drag acceleration of particles in the $100-\mu$ range of diameters requires the use of a very long nozzle, which results in very thick (nearly merged) boundary layers. In the program, the boundary layer calculation is coupled to the one-dimensional channel flow calculation, but the particle acceleration calculation is not coupled; i. e., the particle acceleration occurs in a predetermined gas dynamic flow field and does not affect that flow field.

A solution for one-dimensional channel flow with wall friction and heat transfer is obtained by integration of the following three conservation equations and an equation of state:

Conservation of mass:

$$\frac{dp}{\bar{\rho}} + \frac{d\bar{V}}{\bar{V}} + \frac{dA}{A} = 0 \quad (1)$$

Conservation of momentum:

$$\bar{\rho} \bar{V} \frac{d\bar{V}}{dx} + \frac{dp}{dx} = - 2 c_f \bar{\rho} \frac{\bar{V}^2}{D} \quad (2)$$

Conservation of energy:

$$\bar{V} \frac{d\bar{V}}{dx} + \frac{dh}{dx} = - 4 \frac{c_h}{D} (\bar{h}_t - h_w) \quad (3)$$

Equation of state:

$$\bar{h} = \bar{h}(p, \bar{\rho}) \quad (4)$$

where the skin friction coefficient and the Stanton number are given by the following relations for turbulent flow:

$$C_f = C_1 \left(\frac{\bar{h}}{h_t} \right)^{C_2} \left(\frac{h_w}{h_t R_{ex}} \right)^{C_3} \quad (5)$$

$$C_h = 0.53 C_f \quad (6)$$

The original VKF program was formulated for use with either air, helium, or hydrogen as the gas flow. The properties of high temperature air are obtained from a real gas subroutine which computes equilibrium composition and thermodynamic properties with corrections for intermolecular forces. Helium is treated as an ideal gas, and hydrogen is modeled as a gas which vibrates but does not dissociate. The constants in the skin friction relation were determined from an empirical correlation of test data on turbulent, flat plate boundary layers and are given in Table 1.

Table 1. Constants in Skin Friction Relation Eq. (5)

GAS	C ₁	C ₂	C ₃
AIR	0.15	0.40	0.20
HELIUM	0.068	0.60	0.15
HYDROGEN	0.15	0.50	0.15

Integration of the foregoing equations gives the flow solution in terms of average values ($\bar{\rho}$, \bar{h} , \bar{V}) in a channel of known geometry, with skin friction and heat transfer at the walls of the channel. Corresponding "core flow" values are obtained from an isentropic solution (no skin friction or heat transfer) for the same pressure distribution. Then, the boundary-layer growth from the wall to the

core is obtained by integration of a differential equation for momentum thickness and by reference to two supplemental equations for total thickness and displacement thickness:

$$\frac{d\theta}{dx} + \theta \left[\frac{1}{\rho} \frac{dp}{dx} + (2 + \frac{\delta^*}{\theta}) \frac{1}{V} \frac{dv}{dx} + \frac{1}{D} \frac{dD}{dx} \right] = \frac{C_f}{2} \quad (7)$$

$$(1 - \frac{2\delta^*}{D})^2 = \frac{\bar{\rho} \bar{V}}{\rho V} \quad (8)$$

$$\delta = \delta^* + 6.4 \theta \quad (9)$$

The relation for total thickness was based on experimental data in long, narrow channels. The complete quasi-one-dimensional solution for the channel is obtained by solution of Eqs. (1) to (9). The solution is valid until the boundary-layer growth is great enough that the total thickness merges on the flow centerline. The increase in entropy which would occur downstream of this point is not allowed for in the program as presently constructed.

The behavior of particles in the given flow field is obtained by integration of differential equations for acceleration and particle temperature:

$$\frac{dv_p}{dx} = \frac{C_D A_p \rho (v - v_p) \times |(v - v_p)|}{2 v_p m_p} \quad (10)$$

$$\frac{dT_p}{dx} = \frac{\dot{Q}_p}{(\rho v C_p)_p v_p} = \frac{\rho (v - v_p)}{(\rho v C_p)_p v_p} \frac{C_p (T_o - T_p)}{m_p} \frac{C_{hp}}{v_p} s_p \quad (11)$$

where

$$C_{hp} = \frac{(Nu)}{Re_p} = \frac{2.0 + 0.6 Re_p}{Re_p} \quad (12)$$

by assuming $\text{Pr} = 1$ and

$$\text{Re}_p = \frac{\rho (V - V_p) D_p}{\mu} \quad (13)$$

and the gas temperature is based on the slip velocity. The particle Nusselt number was obtained from Ref. 3 and is strictly valid only for subsonic slip Mach numbers. The relatively large particle diameters used in the present study result in supersonic slip velocities. To allow for this, the particle Reynolds number and heat transfer are simply evaluated using total conditions behind the particle bow shock.

The program version used in the present study was modified from that of Ref. 2 by the addition of the particle temperature history (Eq. (11)) and by extension of the particle acceleration and temperature solution to an arbitrary point in the subsonic region upstream of the nozzle throat. The boundary-layer growth, however, is still assumed to begin at the nozzle throat in order to simplify prediction of mass flow in the nozzle.

2.2 TWO-DIMENSIONAL TRAJECTORY CALCULATIONS IN PARTICLE/GAS FLOW

In the analysis of feasibility of a combined ablation and erosion facility, it was necessary to perform particle/flow calculations for the case in which the slip velocity is not aligned with the particle velocity. In this case, the particles follow curved paths, and a two-dimensional program is required. In this program, as in the one-dimensional program, the particle accelerations are computed in a predetermined flow field, with no coupling of the particle motion upon the flow field. The particle trajectories are obtained by integration of the vector equation of particle acceleration:

$$\frac{d\vec{v}_p}{dt} = \left(\frac{3}{4} \frac{C_D}{D_p} \frac{\rho}{\rho_p} V_s^2 \right) \frac{\vec{V}_s}{V_s} \quad (14)$$

where \vec{V}_s is the slip velocity vector ($\vec{V} - \vec{V}_p$). Since the drag force and acceleration vector are in the direction of \vec{V}_s , the components of acceleration are:

$$\frac{dv_{px}}{dt} = \left(\frac{v_{sx}}{V_s} \right) \frac{dv_p}{dt} \quad (15)$$

and

$$\frac{dv_p}{dt} = \left(\frac{v_s}{v_p} \right) \frac{dv_p}{dt}$$

In this integration, it is considered that D_p and ρ_p are constant, but that C_D , ρ , and v_s are functions of position coordinates depending on the nature of the flow field. Programs for two-dimensional trajectory calculations have been constructed for the following flow fields:

- a. Uniform flow.
- b. Prandtl-Meyer expansion flow.

Conditions along successive expansion rays are calculated by integrating the following expression from known initial conditions:

$$\frac{v_2}{v_1} = \exp \left[\cos^{-1} \left(\frac{1}{M_2} \right) - \cos^{-1} \left(\frac{1}{M_1} \right) + \int_{\alpha_1}^{\alpha_2} \frac{d\alpha}{\sqrt{M^2 - 1}} \right] \quad (16)$$

where α is the angle of an expansion ray measured from the horizontal. The integration is performed numerically, since the real gas effects which dominate the area of interest preclude analytical integration.

- c. Ablation/erosion nozzle flow.

In one comprehensive program, a real gas isentropic expansion of air from high temperatures is calculated and matched in static pressure to a helium or hydrogen flow downstream of an oblique shock. Then, in the same program, conditions upstream of the shock in the light gas are calculated and also conditions downstream of a similar shock in the airflow are calculated. Finally, trajectories of particles having different velocities and diameters are calculated for traversal of the four separate but adjoining flow fields.

2.3 PARTICLE DRAG COEFFICIENTS

For lack of a more workable procedure, the drag coefficients used in most analyses of particle flows are assumed to be those of smooth spheres. In many cases, the particle diameter is such that the slip velocities are low subsonic, in which case the well-established incompressible sphere drag curve giving C_D as a function only of Re_D is used. This curve becomes asymptotic to the Stokes drag coefficient, $C_D = 24/Re_D$, at very low Reynolds numbers (Fig. 3). In the present case, the particle dia-

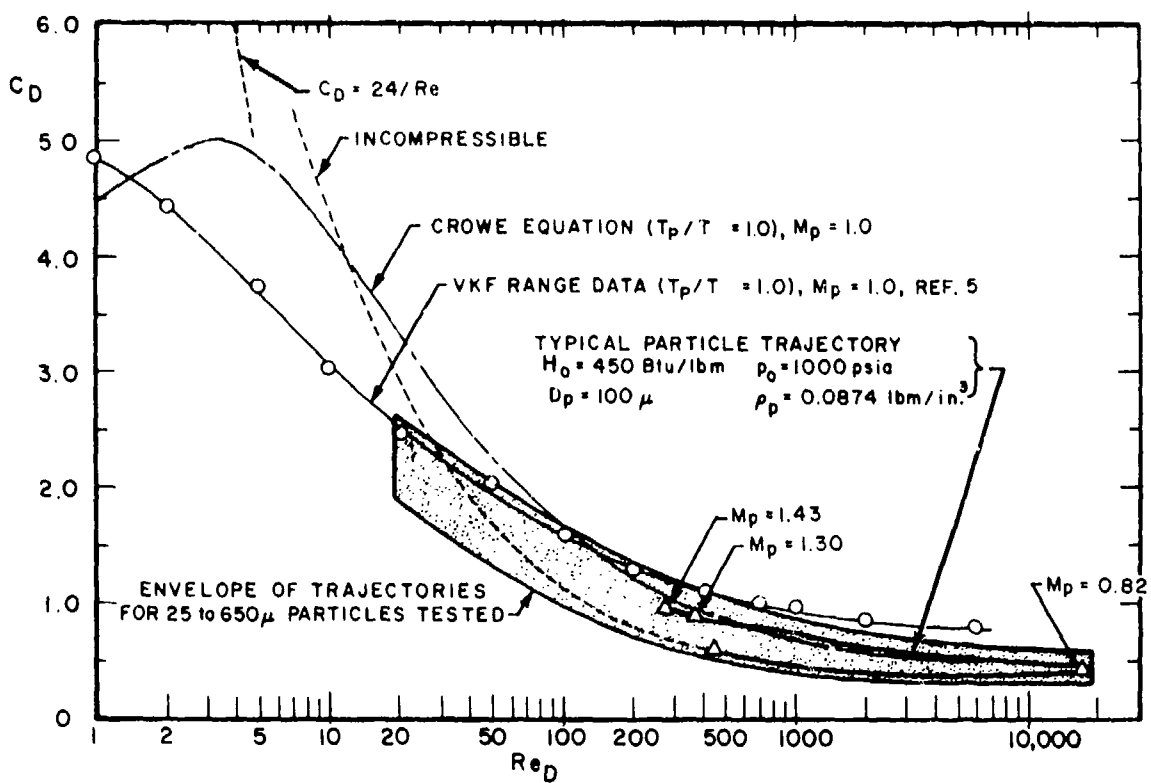


Figure 3. Sphere drag coefficient versus Reynolds number.

ters were such that supersonic slip velocities were often encountered, and it was necessary to recognize the Mach number dependence as well as the Reynolds number dependence of the drag coefficient.

2.3.1 Crowe Drag Correlation

One widely used relation for sphere drag coefficient in the compressible case is that published by Crowe (Ref. 4). This correlation was based on sphere drag data from a large number of different test facilities and is as follows:

$$C_D = (C_{D_{inc}} - 2) \exp \left[-3.07 \gamma^{0.5} \frac{M}{Re} g(Re) \right] + \frac{h(M)}{\gamma^{0.5} M} \exp \left[-\frac{Re}{2M} \right] + 2 \quad (17)$$

$$\log_{10} g(Re) = 1.25 \left[1 + \tanh(0.77 \log_{10} Re - 1.92) \right] \quad (18)$$

$$h(M) = \left[2.3 + 1.7 \left(\frac{T_p}{T} \right)^{0.5} \right] - 2.3 \tanh(1.17 \log_{10} M) \quad (19)$$

where CD_{inc} is the (nearly) classical incompressible drag coefficient of a sphere. Most of the preliminary analyses of this report utilized this drag correlation. It was found, however, that in some regimes the Crowe relation did not agree with AEDC sphere drag measurements (Fig. 3).

2.3.2 Correlation of AEDC Sphere Drag Data

A large amount of sphere drag test data has been obtained at AEDC during the last decade, covering a very large range in Mach number and Reynolds number in the same test facility, a fact which results in a high degree of internal consistency and, inferentially, a high level of absolute accuracy. In Ref. 5, data were published for $0.1 < M < 6.0$ and $20 < Re_D < 100,000$, with effects of sphere temperature given for $M = 2$ to 6 . Further data were reported in Ref. 6 for $0.052 < M < 0.60$ and $0.03 < Re_D < 1000$. A comparison of these data (supplemented by Ref. 7) with Eq. (17) evaluated for $M = 1$ is shown in Fig. 3. As indicated here and in Ref. 9 as well, the use of Eq. (17) can result in drag coefficients which differ substantially from test data at Re_D below 100.

A curve fit was, therefore, obtained for the AEDC test data:

$$CD = \exp \left\{ a_2 (\ln Re_D)^2 + a_1 \ln Re_D + a_0 \right\} \left(1 + k \ln \frac{T_p}{T} \right) \quad (20)$$

with different coefficients obtained for various Mach number ranges (Table 2) and where k is a function of both M and Re_D .

Table 2. Interim Curve-Fit to Sphere Drag Coefficients

(VKF RANGE DATA, REF. 6)
 $M = 0.75-4.2 \quad Re_D = 20 \text{ to } 5000 \quad CD = \exp \left\{ a_2 (\ln Re_D)^2 + a_1 \ln Re_D + a_0 \right\} \quad a_2 = b_2 M^2 + b_1 M + b_0$
 $a_1 = c_2 M^2 + c_1 M + c_0$
 $a_0 = d_2 M^2 + d_1 M + d_0$

M	a_2			a_1			a_0		
	b_2	b_1	b_0	c_2	c_1	c_0	d_2	d_1	d_0
0.75-0.915	0	0.1463	-0.0788	0	-1.557	0.5161	0	4.872	-1.159
0.915-0.965	0	-0.9728	0.9452	0	13.165	-12.95	0	-41.90	41.64
0.965-0.99	0	-0.4661	0.4562	0	5.905	-5.948	0	-12.75	13.50
0.99-1.034	0	1.0218	-1.0168	0	-13.326	13.090	0	42.88	-41.57
1.034-1.135	0	-0.2406	0.2885	0	3.1082	-3.903	0	-9.330	12.42
1.135-1.375	-3.506 ⁻²	9.247 ⁻²	-4.472 ⁻²	-0.6784	1.821	-1.568	3.862	-10.24	8.481
1.375-4.2	5.322 ⁻⁴	-6.427 ⁻³	2.2595 ⁻²	-1.9312 ⁻²	0.1715	-0.5294	8.139 ⁻²	-0.7316	2.506

A comparison of the curve fit with test data is given in Fig. 4 for two different Mach numbers.

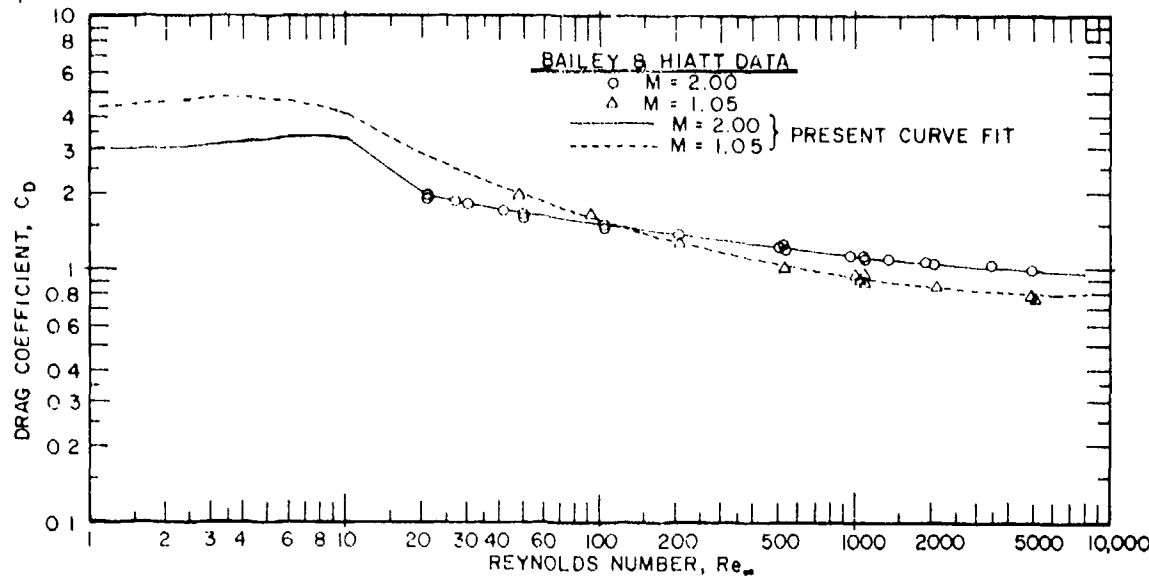


Figure 4. Comparison of curve fit and AEDC data on sphere drag coefficient.

2.3.3 Nature of "Real" Particles

Both of the empirical drag correlations described above are strictly valid only for single, smooth, spherical particles. However, real particles used in testing often display very nonspherical shapes and a fairly broad distribution of sizes (Fig. 5 and 6). In practice, then, one would expect to observe a dispersion of results about a "mean" velocity or trajectory calculated for an effective average spherical particle. Note that it would be possible for effects of nonsphericity on drag to be compensated by errors in determination of the particle sizes.

The particle samples formed of small glass beads (Figs. 5 and 6) were used to reduce the dispersion of results for careful calibration work. Experimental measurements of particle behavior invariably show this reduction in dispersion.

3.0 EXPERIMENTAL EVALUATION OF GAS/PARTICLE FLOW PROGRAMS

Adequacy of the gas/particle flow programs as design tools was evaluated in several different experimental programs, some designed specifically for the evaluation and some designed for other purposes.

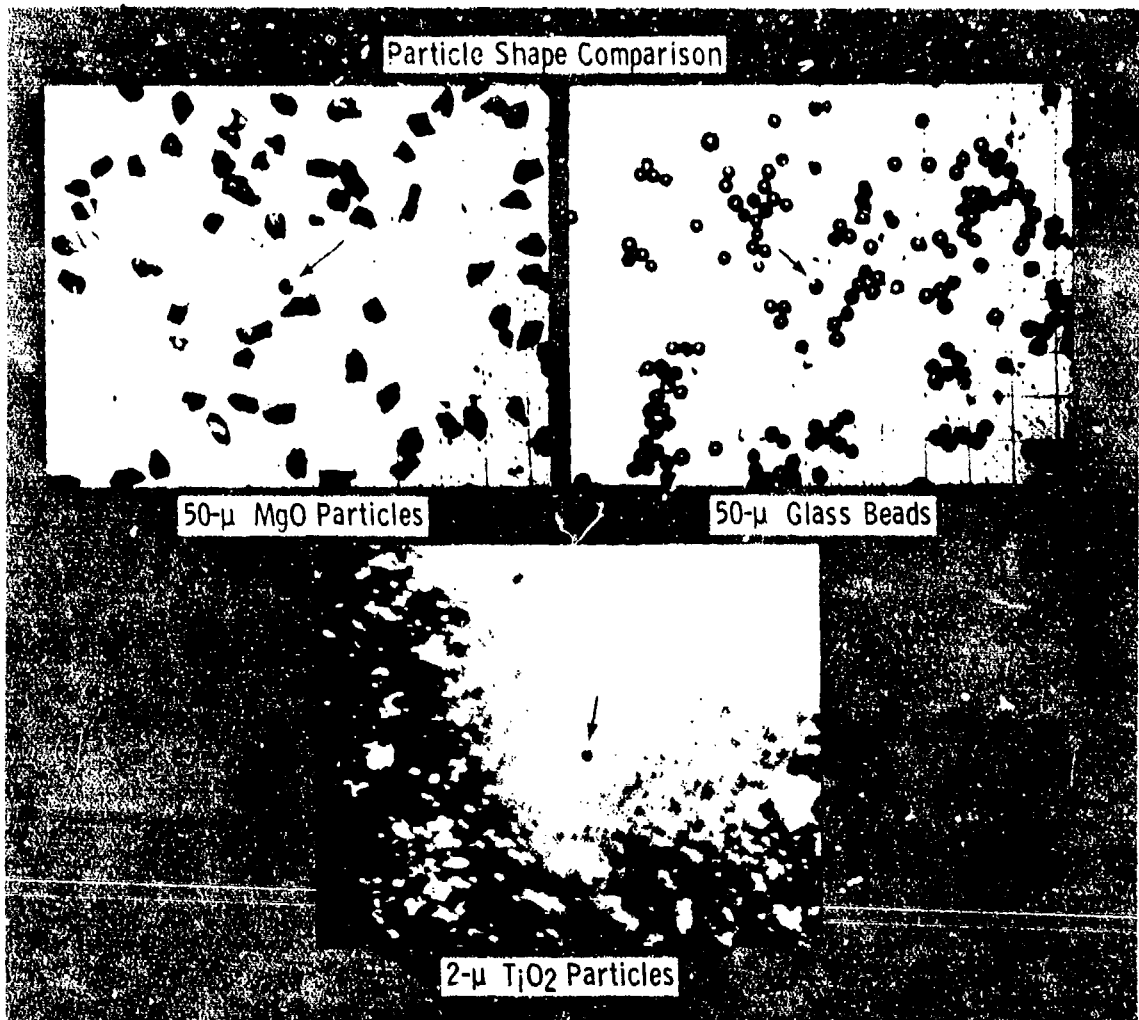
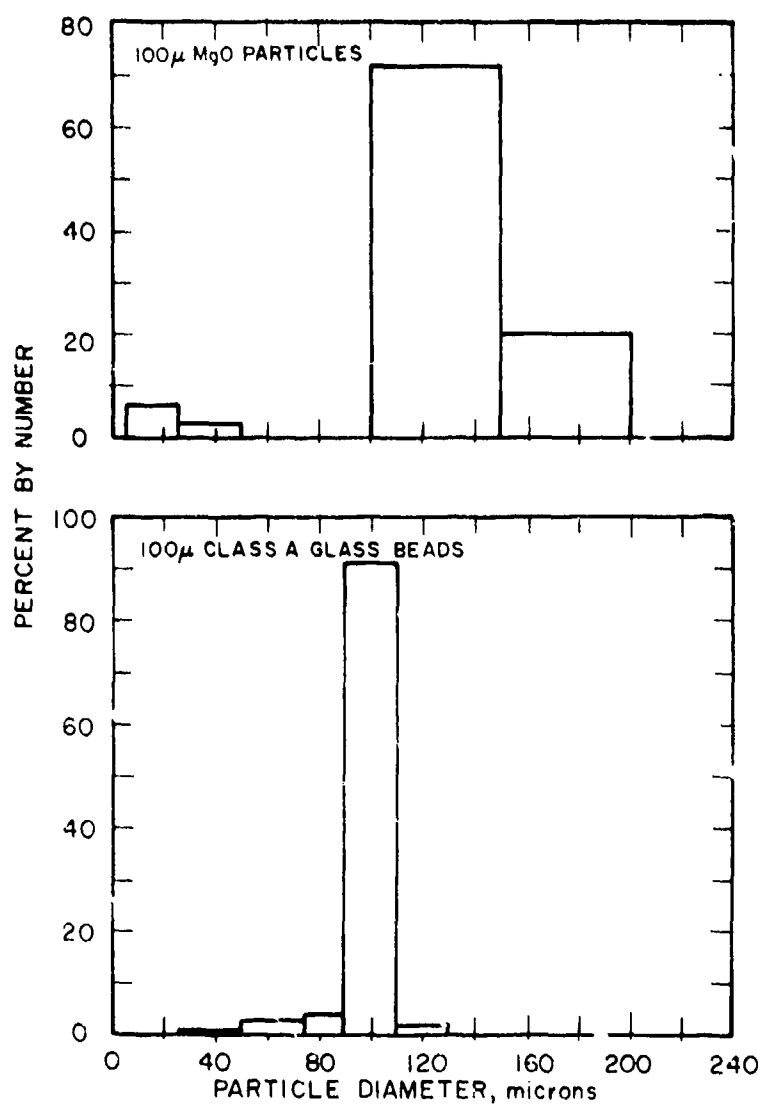


Figure 5. Photomicrographs of particle samples showing individual shapes.

3.1 EVALUATION OF THE ONE-DIMENSIONAL PARTICLE ACCELERATION PROGRAM

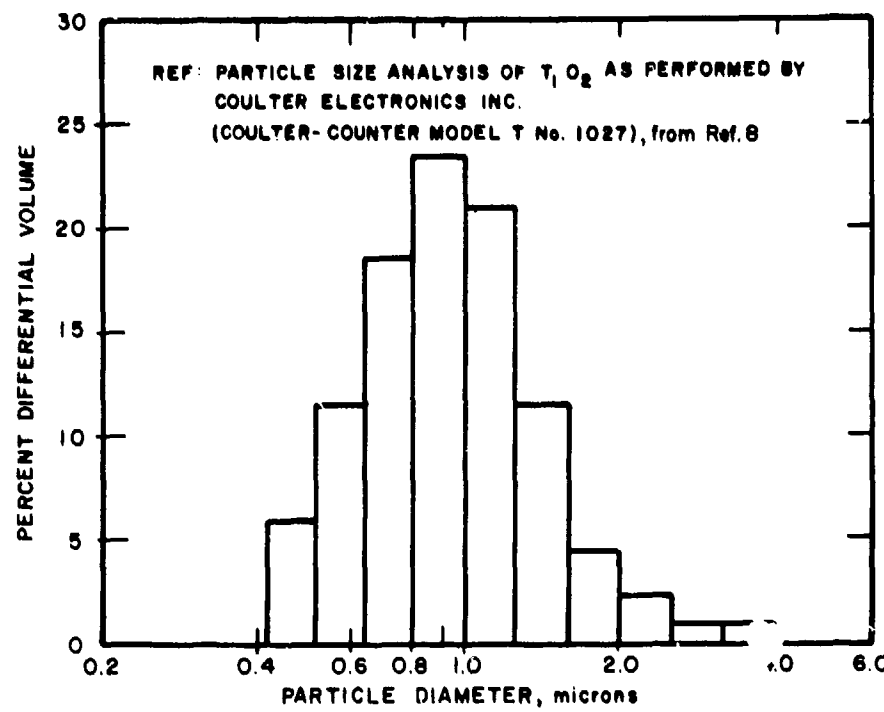
Uncertainties contained in the particle acceleration program include the drag coefficient correlation, the boundary-layer calculation for very thick boundary layers, and in the case of air, the high temperature thermodynamic property routine. The experimental evaluations were made under conditions in which the various uncertainties were present at the same time. Therefore, only an overall evaluation of the program was possible, not a separate evaluation of the individual uncertainties.



a. 100- μ MgO particles and 100- μ glass beads
Figure 6. Particle size histograms.

3.1.1 PWT Dust Erosion Tunnel (DET)

The DET was designed in 1970 as an arc-heated wind tunnel having high-speed particle capability. The acceleration nozzle for this facility was designed using the unmodified version of the one-dimensional program (Section 2.1). This nozzle has a throat diameter of 0.563 in., an exit diameter of 15.34 in., and length of 209 in. The modified program was recently applied to this nozzle, and the results are given in Fig. 7.

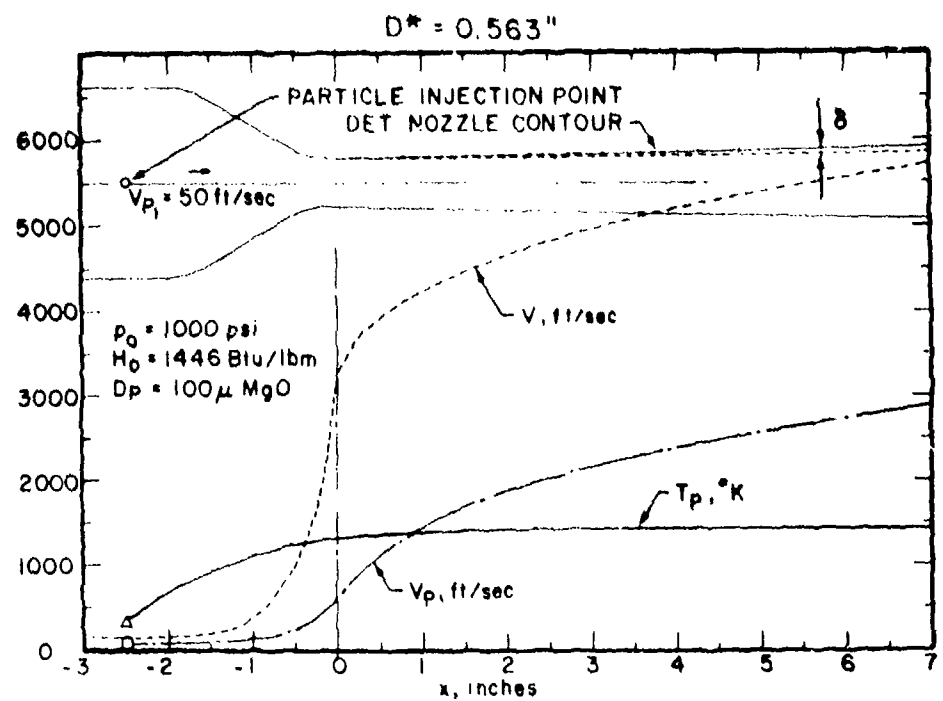


b. $1-\mu$ TiO_2 particles
Figure 6. Concluded.

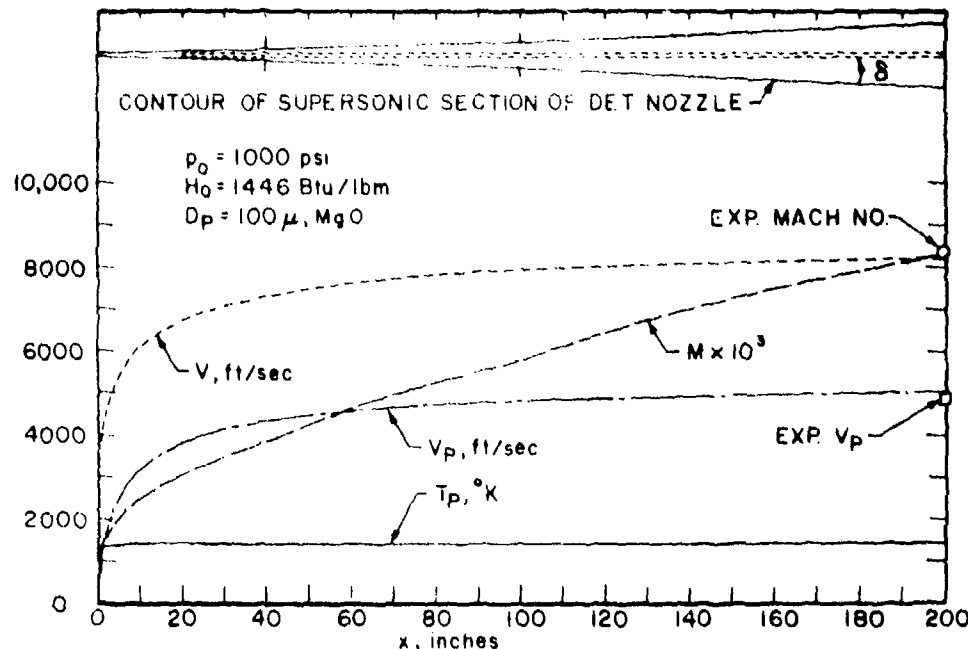
The gas velocity, the velocity and temperature of $100-\mu$ magnesium oxide particles, and the gas Mach number are shown as functions of distance along the nozzle for $p_0 = 1,000$ psi and $H_0 = 1,446$ Btu/lbm.

The experimental Mach number at the nozzle exit was determined by measurement of the impact pressure and the nozzle static pressure and was found to be very close to the value predicted by the one-dimensional program (Fig. 7b). The impact pressure profiles (not shown here) also verify that the exit flow is very close to the merged boundary-layer condition.

Particle velocities were measured at the nozzle exit by double-pulse optical holography, and the dispersion in velocity because of variations in particle size was clearly observed. However, the mean value of 4,900 ft/sec was very close to the value of 5,000 ft/sec predicted for $100-\mu$ particles. The predicted gas velocity was 8,250 ft/sec. The velocities measured for different diameter particles are compared with the one-dimensional program predictions using both drag coefficient correlations in Fig. 8.



a. Throat region



b. Supersonic section

Figure 7. Gas velocity, Mach number, particle velocity, and temperature in DET nozzle, $D^* = 0.563$ in.

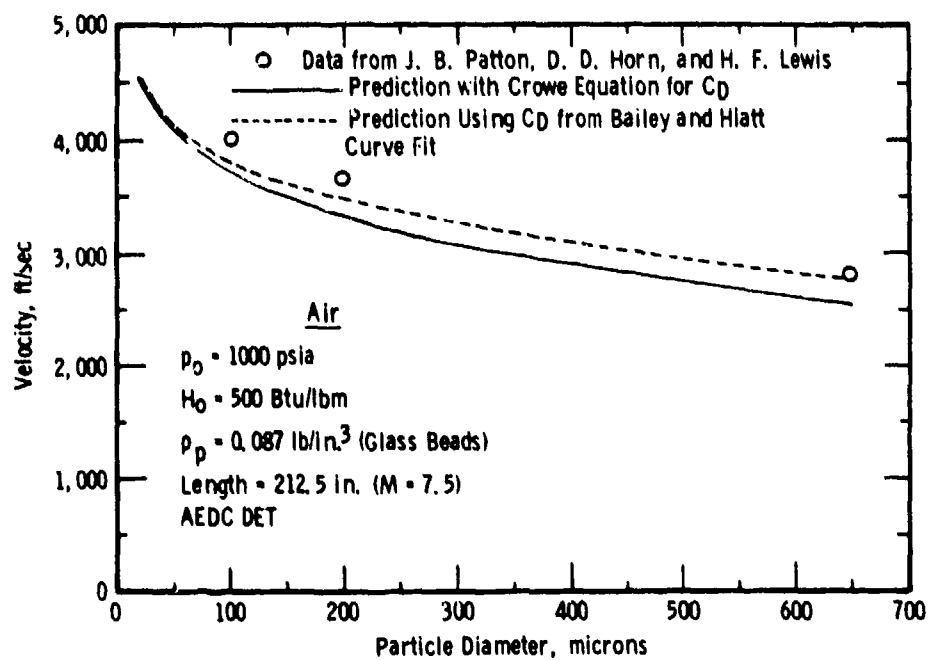


Figure 8. Comparison of calculated and measured particle velocities in DET.

3.1.2 Light-Gas Acceleration Nozzle

To evaluate the performance of the light-gas accelerator in the proposed ablation/erosion nozzle, the one-dimensional program was applied to a small nozzle having a large L/D ratio. This nozzle was a simple conical nozzle having a 0.5-deg divergence half-angle and a throat diameter of 0.119 in. Results of the calculation for a helium expansion from $p_0 = 1,000 \text{ psi}$ and $T_0 = 2,000^\circ\text{R}$ are shown in Fig. 9, for a range of particle diameters from 10 to $1,000 \mu$. The nozzle dimensions and reservoir conditions for this calculation were selected on the basis of equipment availability. For $100-\mu$ particles, a velocity of 4,500 ft/sec is attained at a length of 18 in., very close to that attained in the DET in a length of over 200 in. and for an accelerating gas stagnation temperature only 40 percent that of the DET. The calculation also indicates, however, a boundary-layer merge at a distance of 14 in. As noted in Section 2.1, the gas dynamic part of the program is not strictly valid downstream of this point; however, it is believed that the particle acceleration calculations will not be seriously affected for an appreciable distance downstream of this point.

In Fig. 10 is shown the particle velocity variation in the same nozzle, calculated with both of the drag coefficient correlations of

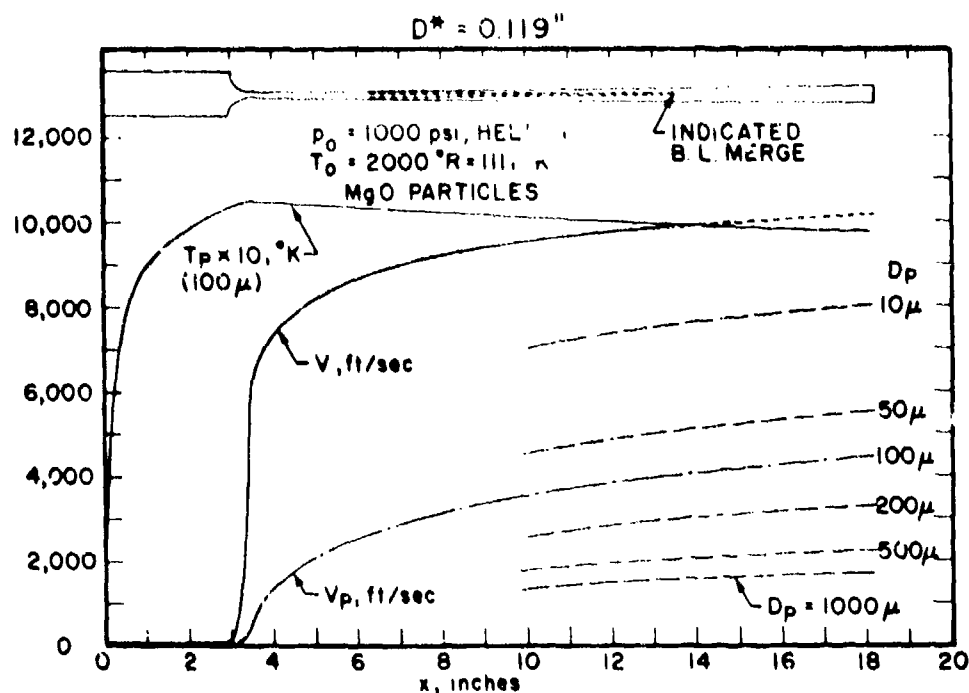


Figure 9. Gas velocity, particle velocity, and temperature in helium acceleration nozzle, $D^* = 0.119$ in.

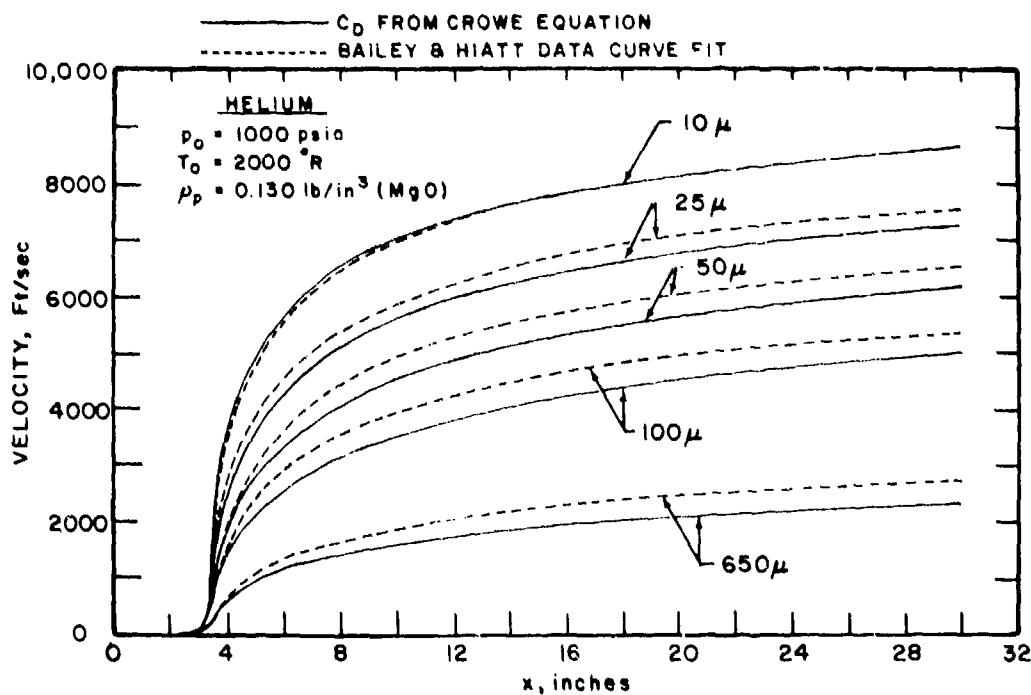


Figure 10. Calculated particle acceleration in light-gas particle acceleration, helium.

Section 2.3. The drag correlation based on the AEDC test data (Eq. (20)) gives particle velocities approximately 10 percent higher than does the correlation of Eq. (17).

3.1.2.1 Experimental Apparatus for Light-Gas Acceleration

An experimental apparatus was assembled, including an available electric resistance heater, a stilling chamber and particle injection system, a particle acceleration nozzle, various instrumentation systems, and a helium and air gas supply system.

The resistance heater was essentially a carbon steel shell with an inner stainless steel liner in which a spiral-wound coil of Kanthal® wire was mounted, properly insulated with Fibre Frax®. The design conditions for this heater were 1,000 psi and 2,000°R. Electrical resistance of the heating element was approximately 2 ohms. The heater was operated with a d-c power supply having two ranges of operation: 4,000 amp at 250 v and 2,000 amp at 500 v. A ballast resistor of 0.4 ohm was used in the heater circuit. Performance of this heater was calibrated with air for mass flows of 0.16 to 0.3 lbm/sec and output temperatures up to 1,800°R. The heater was not calibrated with helium because of the cost involved, but results observed in operation of the acceleration nozzle with helium indicated that approximately the same temperatures were attained as with air.

The 1-in.-ID stilling chamber (Fig. 11) was machined from a stainless steel bar and was attached to the resistance heater by a short length of stainless steel tubing. Provision is made in the stilling chamber for

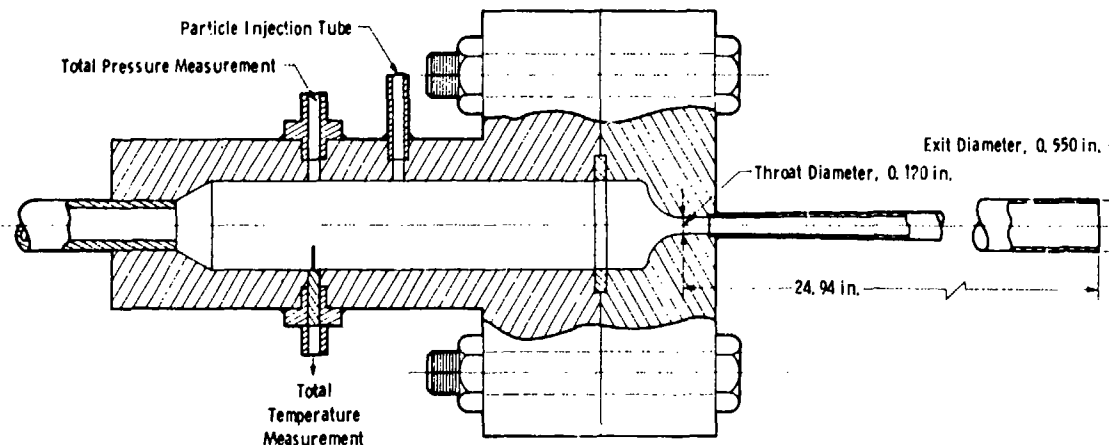


Figure 11. Cross section of stilling chamber and nozzle of light-gas accelerator.

measurement of stagnation pressure and temperature and for introduction of particles.

The particle acceleration nozzle itself (Fig. 11) was made from a tapered tube welded to a throat assembly. The tapered tubes obtained were of Type 347 stainless steel, having a wall thickness of 0.035 in. and a length of approximately 25 in. The tube was cut to the required size and welded to the pre-machined throat block. The nozzle inlet is a circular arc transition to the 0.5-deg divergence angle at the tapered tube. The throat diameter is 0.120 in. and the diameter at the 25-in. length is 0.55 in.

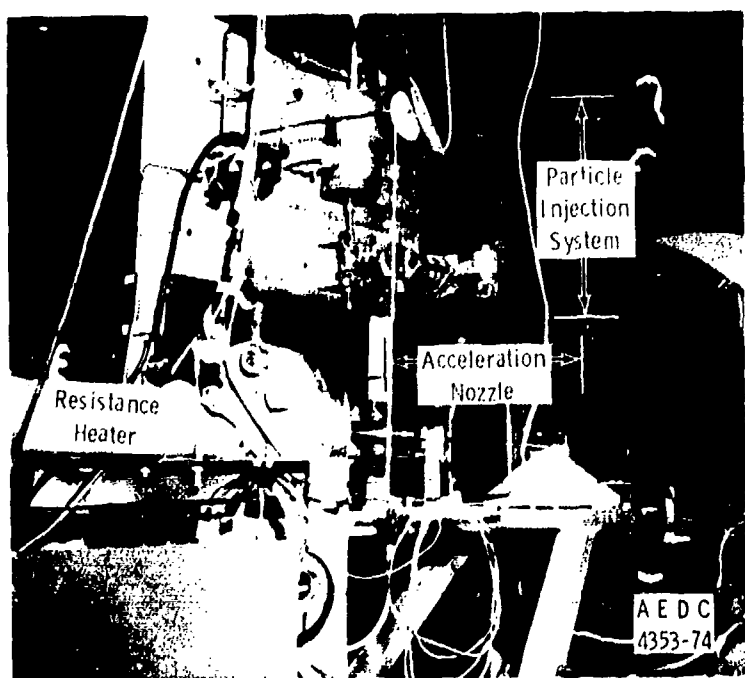
A simple particle injection system was constructed, having a carbon-steel reservoir with an inverted-cone lower surface. This tank was separated from the stilling chamber by a ball valve and metering orifice, pressurized by a regulated helium supply. Particle injection is 90 deg to the axis of the flow; no attempt was made to inject with a velocity component parallel to the flow. A vibrator was added to the system to ensure a smooth and continuous particle flow. The initial configuration of this system provided excessive particle flow rates, but after modification to allow injection under essentially zero pressure difference across the orifices, flow rates as low as 0.0006 lbm/sec were obtained.

Provisions were made for measuring the stagnation conditions in the reservoir. To calibrate the exit flow, a three-probe rake was designed for traversal of the flow. This rake included a metal-sheathed, Chromel[®]-Alumel[®] stagnation point temperature probe, a conventional impact pressure probe, and a static pressure probe. The static pressure probe was eventually removed since very little data were ever retrieved from it. The rake was driven by a low-speed traversing system.

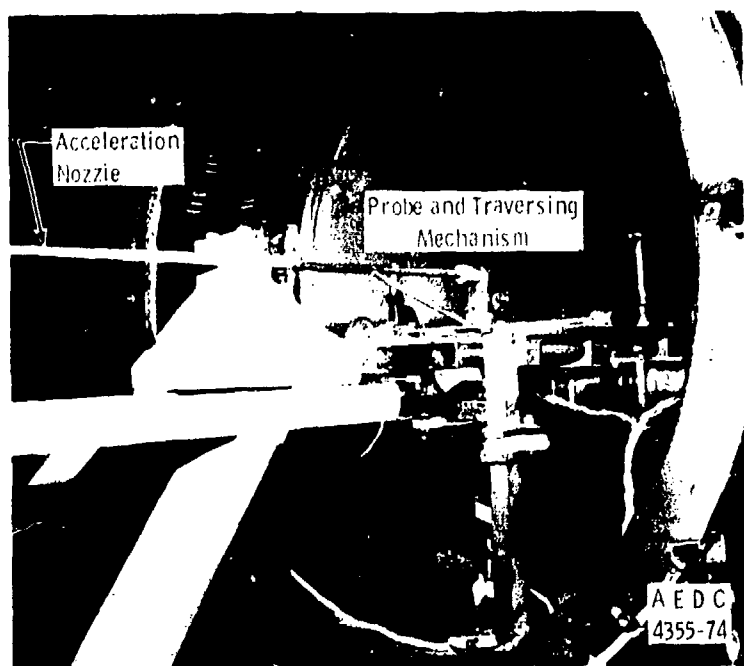
Photographs of various components of the installation are given in Fig. 12.

3.1.2.2 Aerodynamic Calibration

The light-gas acceleration nozzle was calibrated with both air and helium. Changes in nozzle length due to thermal expansion required that the calibration probes be pre-positioned some distance downstream of the nozzle exit. After a 4-min stabilization period, the gap between the probes and nozzle was narrowed to the desired value of 0.10 in.



a. Heater end of apparatus



b. Exit of nozzle

Figure 12. Photographs of light-gas particle accelerator apparatus.

A typical impact pressure profile measured at the nozzle exit for air at $p_0 = 935$ psi and $T_0 = 1,284^\circ\text{R}$ is given in Fig. 13. At this lower T_0 , the nozzle flow should not be merged and a small region of constant impact pressure does appear at the centerline of the profile. Under this condition, it is legitimate to infer a nozzle exit static pressure from the impact pressure and an assumed isentropic expansion on the nozzle centerline. This pressure was assumed to be (essentially) constant over the profile and p/p'_0 used to obtain the Mach number profile, also shown in Fig. 13. The oscillation in the impact pressure profile is believed to be the result of oblique shocks at the nozzle exit due to overexpanded flow conditions.

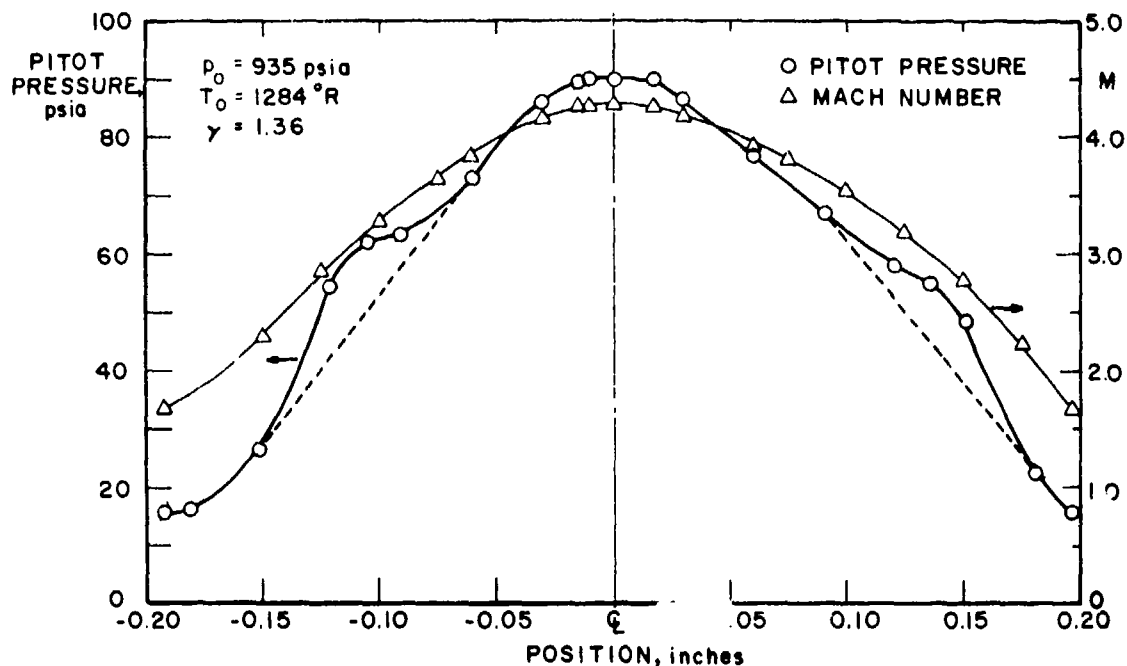


Figure 13. Pitot pressure and Mach number profiles in light-gas particle acceleration nozzle operated with air.

At all lower stagnation temperatures, the boundary layer will be even thinner, so that the same procedure should be valid to obtain the centerline Mach number, shown in Fig. 14 for air as a function of T_0 . The experimental M_C curve is parallel to the inviscid curve (which decreases with T_0 because of real gas effects in air) and roughly half-way between the inviscid curve and the viscous flow solution obtained with the one-dimensional program. The air liquefaction boundary is shown for reference as well as velocities calculated for 50- and 100- μ particles of MgO.

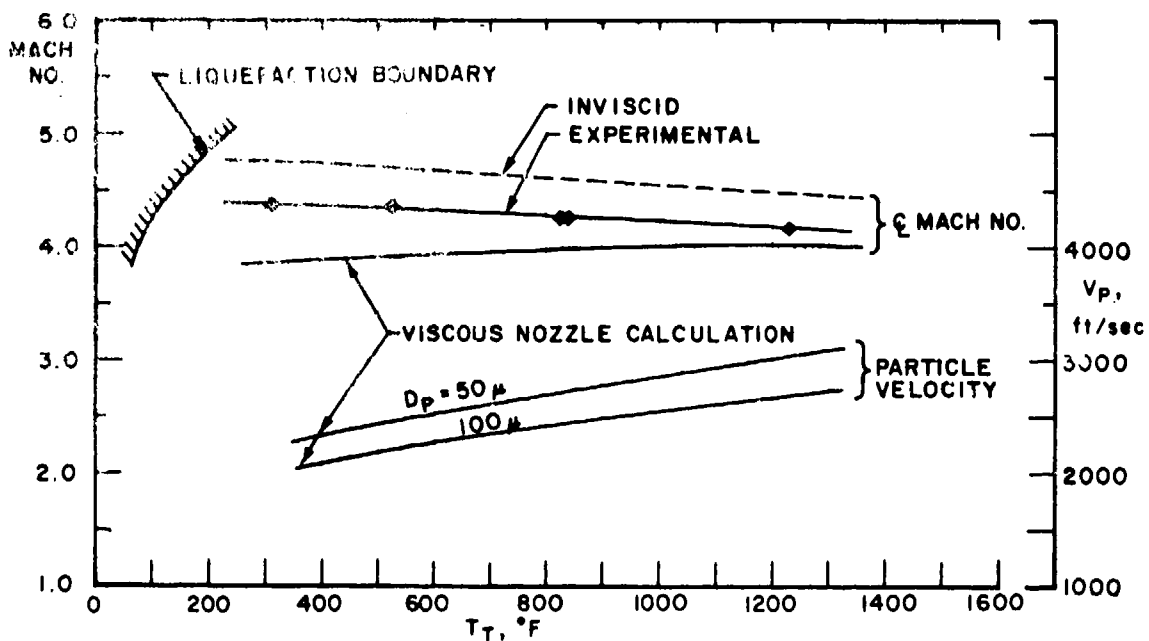


Figure 14. Mach number and calculated particle velocity in light-gas accelerator, air.

Corresponding aerodynamic calibration data obtained with helium at $p_0 = 750$ psi are given in Fig. 15. The experimental Mach numbers again fall between the inviscid line (constant for a perfect gas) and the viscous nozzle calculation; however, in the case of helium, the results are closer to the viscous calculation. The trends are the same as for the calibration with air.

3.1.2.3 Particle Velocity Calibration

During the initial work with the light-gas acceleration nozzle, the only technique available to obtain an indication of high velocities was that of impact specimens. Photographs of two 1/16-in.-diam steel rods exposed to particle flows for periods of 1 sec are shown in Fig. 16. Note the difference between the specimen exposed to 2,700-ft/sec particles of MgO accelerated by air and the specimen exposed to 5,200-ft/sec particles of MgO accelerated by helium. Even specimens exposed to 100- μ glass beads accelerated by cold helium display characteristic hypervelocity impact craters (Fig. 17).

An extensive effort was made to obtain particle velocity measurements by use of the double-pulse holography technique used so successfully in the DET. However, the much higher density and turbulence

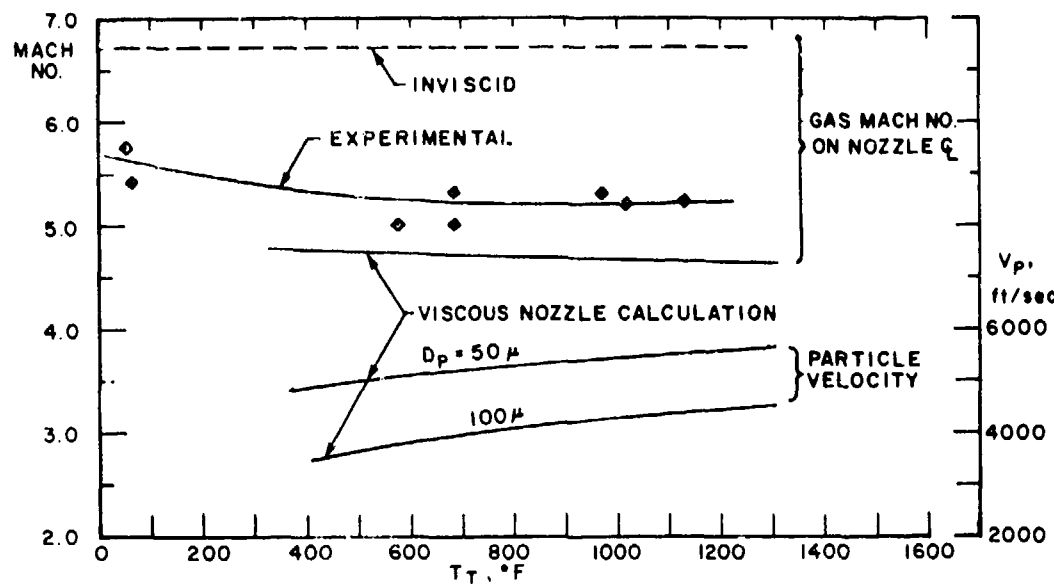


Figure 15. Mach number and calculated particle velocity in light-gas accelerator, helium.

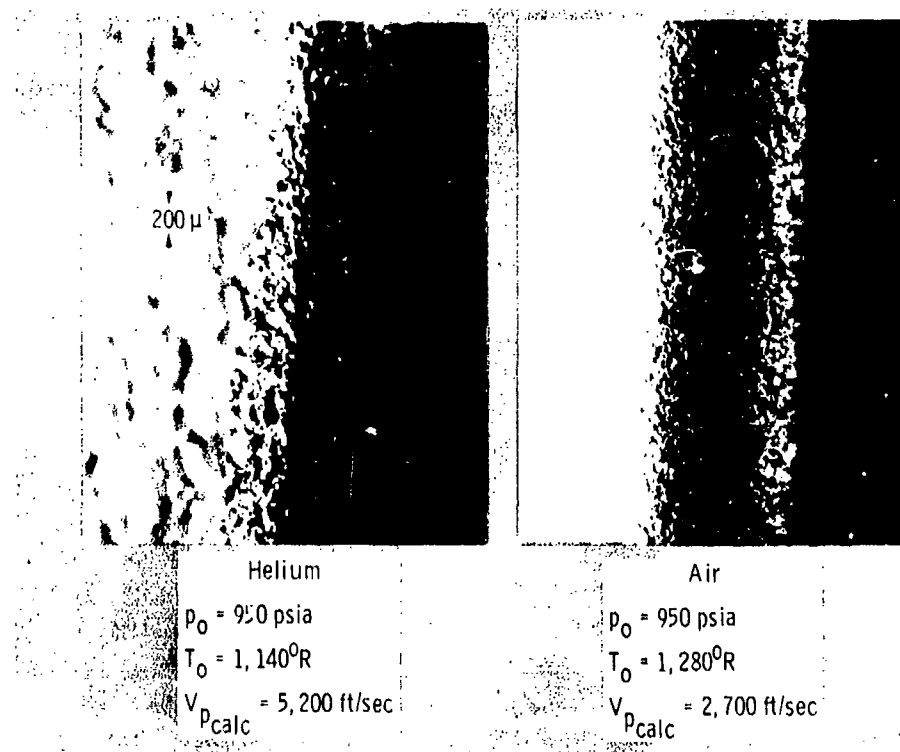


Figure 16. Photographs of impact bars after 1-sec exposure to 50-μ MgO particles, air and helium.

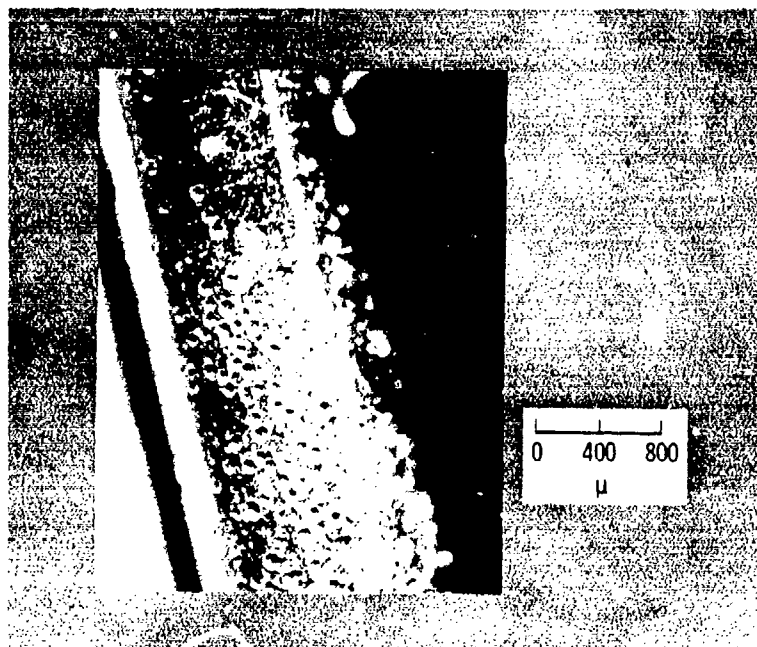


Figure 17. Photograph of impact bar after exposure to 100- μ glass beads at 3,200 ft/sec (calculated).

levels in the light-gas particle acceleration nozzle were found to degrade the object beam to such an extent that the holograms were not reconstructible. Near the end of the project effort, however, velocity measurements were obtained with a laser (doppler) velocimeter which was optimized for the conditions of the light-gas nozzle. As noted below, the velocities measured in the nozzle were close to predicted values.

3.1.2.4 Evaluation of One-Dimensional Program

Ultimately, the one-dimensional program should be judged on the basis of its intended use, namely, to predict the velocities of particles which are accelerated by drag forces in special acceleration nozzles. A summary plot of particle velocities measured by two different techniques in two different facilities, in comparison with values predicted by the one-dimensional program, is given in Fig. 18. This comparison clearly establishes the one-dimensional program as a valuable design tool and appears to eliminate the possibility of any major errors in the drag coefficient routine, the thick boundary-layer formulation, or the real gas routines for air properties. In addition, the agreement of the aerodynamic calibration with predictions of the program is further evidence that the gas dynamic formulation of the program is sound.

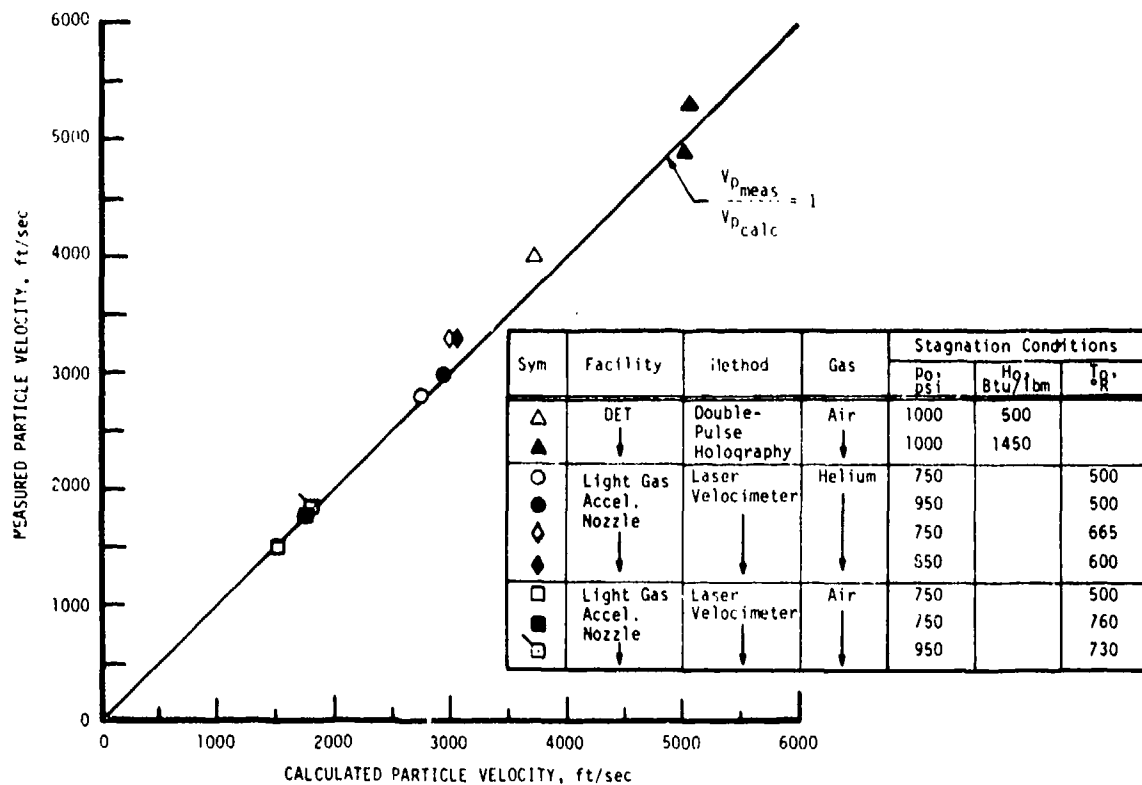


Figure 18. Summary of particle velocity measurements in DET and light-gas particle acceleration nozzle, 100- μ MgO particles.

3.2 TWO-DIMENSIONAL TRAJECTORY EXPERIMENT IN THE DUST EROSION TUNNEL

Analytical trajectories computed for particles in various flow fields suggested that particles of 100- μ diameter, when moving at velocities of thousands of feet per second, are very insensitive to deflection by the flow fields. Since such behavior could be of very great use in operation of a combined ablation/erosion nozzle, experimental verification of this was considered to be of substantial importance. An experiment was designed for this purpose in which particles would be subjected to a cross flow created in Prandtl-Meyer expansion formed in the DET.

The DET facility (Fig. 19) provides particle flow at high velocity in a nozzle which may be operated at several lengths, the extremes producing Mach numbers of 5.9 and 9.47. This facility operates with a 5-MW arc heater providing reservoir conditions of 1,000 psi and enthalpy from 400 to 2,000 Btu/lbm.

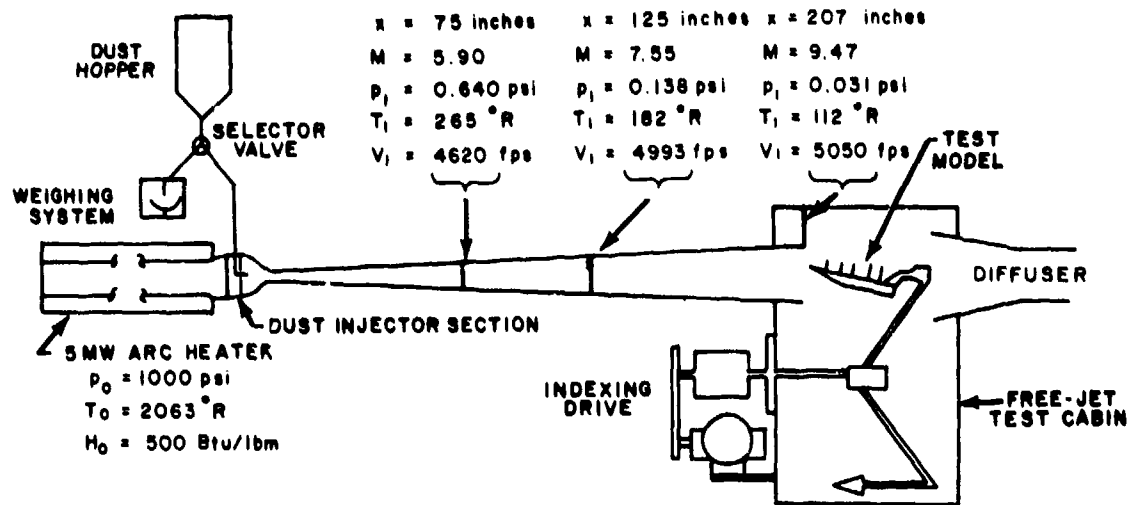


Figure 19. Schematic of AEDC/PWT Dust Erosion Tunnel (DET).

An adjustable wedge model was designed and fabricated from stainless steel (Fig. 20). By varying the angle of attack of this model, a Prandtl-Meyer expansion flow of desired strength could be generated on the lee side of the model. The wedge tip is replaceable, and up to ten 3/16-in.-diam impact bars were mounted on the lee surface. The trajectory of particles in the Prandtl-Meyer flow region can be determined by location of the impact boundaries on each successive bar. To the extent that the particles will have a certain spread in size (Fig. 6), shape (Fig. 5), and probably small differences in initial velocity vector, the boundary of the impact zone will be somewhat diffused, increasingly so at the more downstream impact bars.

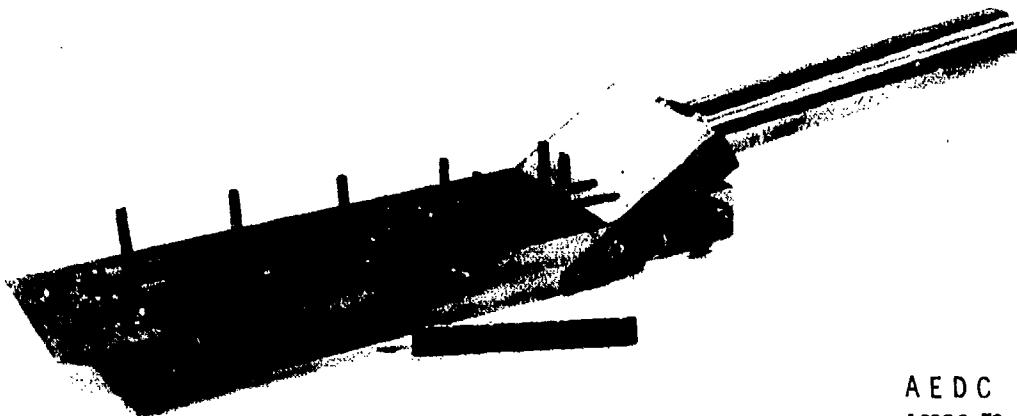
AEDC
10338-73

Figure 20. Photograph of Prandtl-Meyer expansion test model.

Twelve tests of the Prandtl-Meyer flow model were run in the DET (Table 3). The tests performed at $M = 7.5$ were parasite tests performed during operation of the DET for another purpose. They were performed for familiarization only since prior calculations indicated the particle deflections at the $M = 7.5$ condition would not be detectable. When the DET became available for a test dedicated to the particle trajectory study, the model was moved upstream to the $M = 5.5$ station, for which conditions the theoretical analysis indicated that detectable deflections over a 7-in. length would occur. As shown in Table 3, six tests were performed at $M = 5.5$, using glass beads of two different diameters, MgO particles, and TiO_2 particles.

Table 3. Conditions for Prandtl-Meyer Flow Tests in Dust Erosion Tunnel

Test No.	Tunnel Conditions					Particles			Angle of Attack = Prandtl-Meyer Exp. Angle	
	P_0 psi	H_0 Btu/lbm	Mach Number	V_1 ft/sec	P_1 psi	Mat'l	Nominal D_p μ	ρ_p lb/in. ³	Measured Before Run, deg	Calculated from Curve-Fit To Trajectory
1	1014	465	7.55	4815	0.140	MgO	100	0.132	5.20	5.74
2	1004	482	7.55	4902	0.139	MgO	100	0.132	5.27	5.51
3	998	455	7.55	4763	0.138	Glass	650	0.087	7.33	7.83
4	996	473	7.55	4856	0.137	Glass	50	0.087	7.29	7.54
5	1000	513	7.55	5057	0.138	Glass	50	0.087	7.22	7.68
6	996	431	5.9	4289	0.637	Glass	100	0.087	5.57	8.22
7	1002	430	5.9	4284	0.641	MgO	50	0.132	5.35	6.41
8	996	419	5.9	4229	0.637	Glass	25	0.087	5.35	6.26
9	1002	415	5.9	4209	0.641	TiO_2	1	0.147	5.33	5.33
10	350	1750	5.9	8643	0.224	TiO_2	1	0.147	5.35	6.13
11	996	437	5.9	4319	0.637	Glass	25	0.087	5.34	6.53
12	1000	400	7.55	4466	0.138	MgO	100	0.132	5.32	5.82

A photograph of the model after a run is shown in Fig. 21 and a photomicrograph of one of the forward impact bars is given in Fig. 22. The edge of the impact area is clearly evident, even though it is not perfectly sharp. The trajectory was defined by the mean impact point, assumed to lie halfway between the point where there are essentially no impacts and the point where there is judged to be essentially uniform

coverage in the impact zone. This position was measured to a resolution of 0.0001 in. on the photomicrograph. The impact locations were curve-fit to an hyperbola passing through the sharp tip of the model and the model angle of attack was established by a tangent to the hyperbola at the nosetip. In all cases, the model angle of attack determined in this manner was greater than the angle of attack measured before the run, suggesting a deflection due to the air loads during the run. Both angles of attack are given in Table 3.

Particle trajectory data for a typical case are given in Fig. 23. These data are for 25- μ glass beads passing through a 6.53-deg Prandtl-Meyer expansion at $M = 5.5$, with $p_0 = 996$ psi, $H_0 = 437$ Btu/lbm. Based on the one-dimensional program for this case, the gas velocity was 4,302 ft/sec and the particle velocity was 3,900 ft/sec. In this case the cross-stream deflection of 0.0327 in. was slightly less than the predicted deflection of 0.0369 in. at 6.65 in. from the nose of the model.

A summary of predicted cross-stream deflection 6.65-in. downstream of 6.25-deg Prandtl-Meyer corner, for a large range in particle

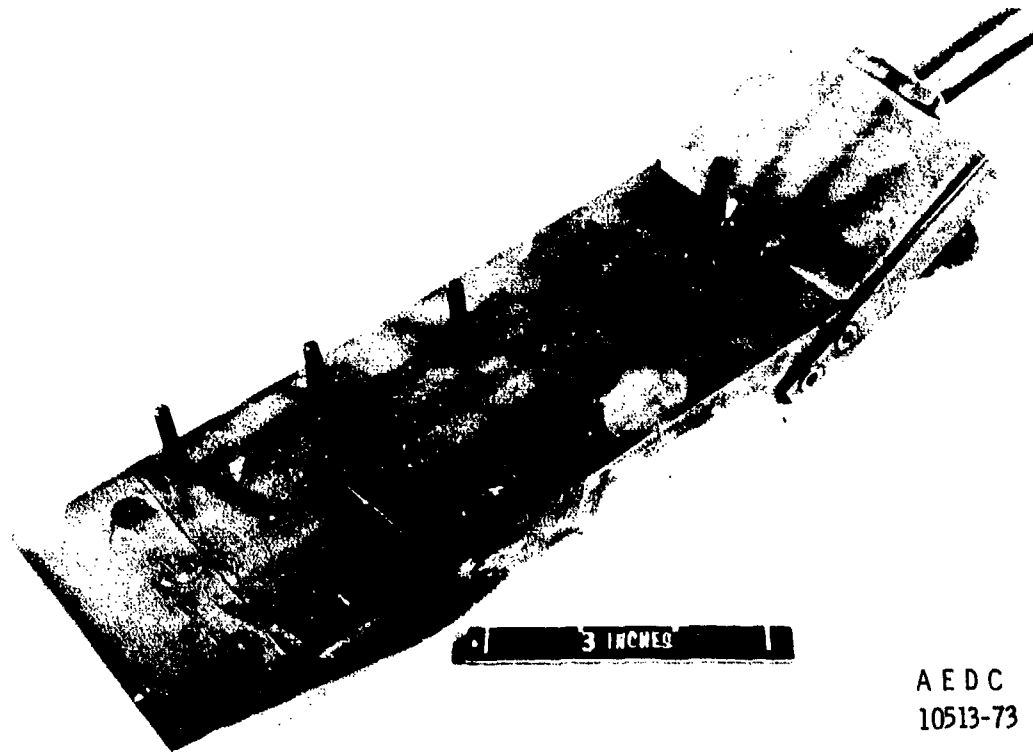


Figure 21. Photograph of Prandtl-Meyer expansion test model after run in DET.

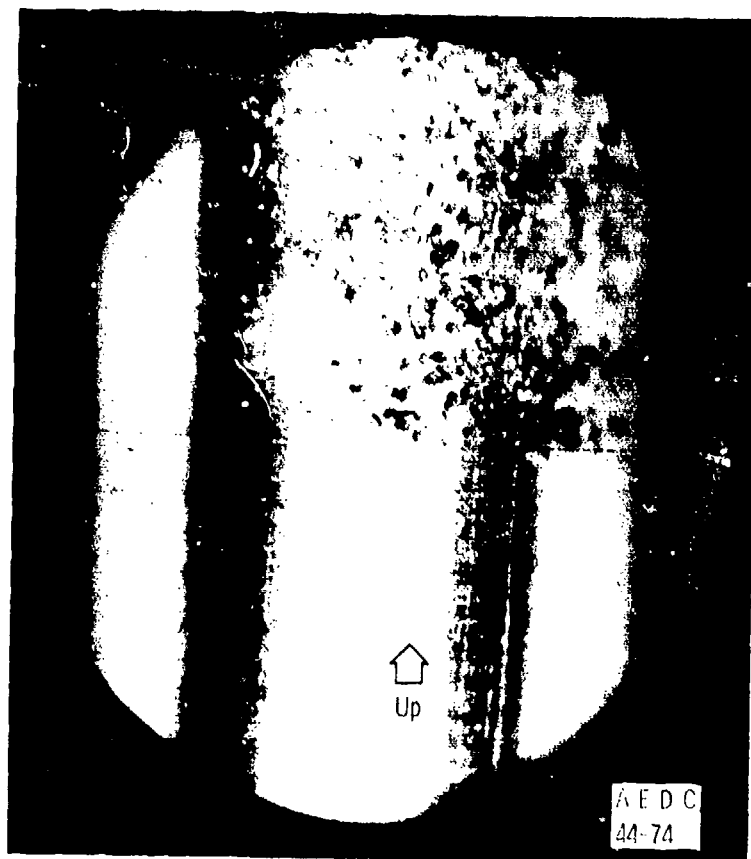


Figure 22. Photomicrograph of impact bar from Prandtl-Mayer test model.

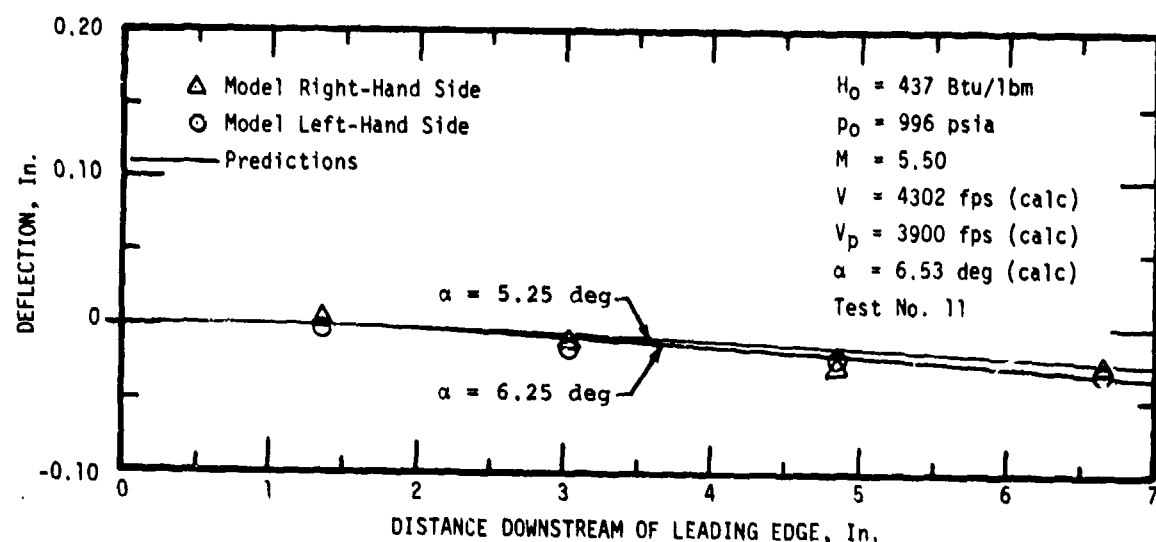


Figure 23. Trajectory measurements for $25\text{-}\mu$ glass beads in Prandtl-Mayer expansion test in DET.

diameters, is given in Fig. 24. The calculations predict all particles with diameters greater than $10\text{-}\mu$ will deflect no more than 0.10 in., representing nearly linear trajectories. All particles having diameters less than $1\text{-}\mu$ will essentially follow the flow streamlines. The transition region covers a fairly narrow decade of diameters between 1 and $10\text{-}\mu$. The experimental points for the beads and the TiO_2 particles are in good agreement with the predictions, but the deflection of the MgO particles of $50\text{-}\mu$ diameter is about three times the predicted value. Except for the single MgO point, the data establish the adequacy of the two-dimensional trajectory program for design purposes. It is not known whether the MgO point is an exceptional point or whether it reflects increased drag due to the irregular shape of the MgO particles. In view of the good agreement of one-dimensional acceleration of MgO particles with calculations, it is not deemed likely that the discrepancy is the result of irregular shapes. The test data appear to confirm the calculations at the extremes of diameters near the limiting cases, but unfortunately, no particle samples were available which would have fallen in the transition regime.

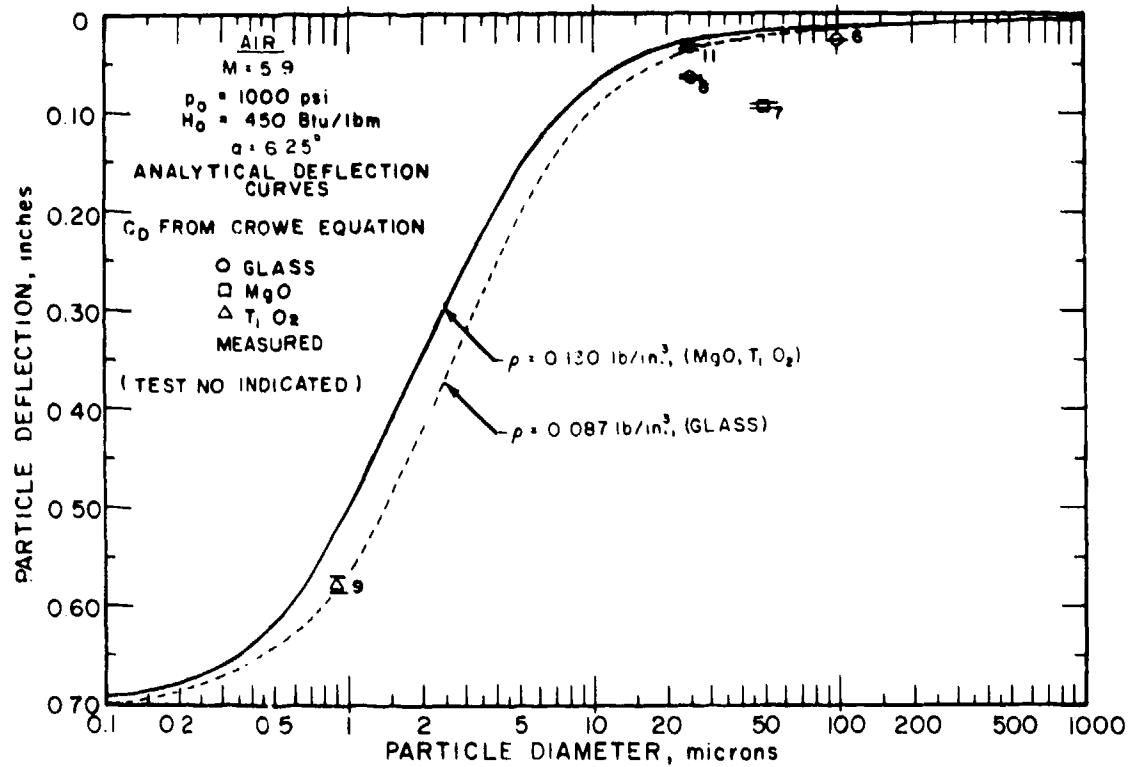


Figure 24. Summary of particle deflection data 6.65 in. from Prandtl-Meyer corner, DET, $M = 5.9$.

4.0 ANALYSIS AND DESIGN OF A COMBINED ABLATION/EROSION NOZZLE

An analysis of the proposed ablation/erosion nozzle was conducted, using as design tools the programs for gas/particle flow described in Section 2.0 and which had been experimentally verified as described in Section 3.0.

4.1 PARAMETRIC DESIGN STUDY OF ABLATION/EROSION NOZZLE

A detailed numerical analysis of the nozzle configuration shown in Fig. 2 was made. The arc-heater reservoir conditions were assumed to be $p_{\infty} = 200$ atm and $H_{\infty} = 2,100$ Btu/lbm, which are representative maximum pressure operating conditions for a typical high-pressure arc heater. The light-gas particle acceleration nozzle was assumed to intersect the arc-heated air nozzle at angles of 10, 15, and 20 deg. The divergence half-angle of the light-gas nozzle was assumed to be 0.5 deg. The initial calculations were made with helium as the light gas and with reservoir conditions of 1,000 psi and 2,000°R.

4.1.1 Flow-Field Analysis

Flow-field conditions upstream and downstream of the helium and air shock waves were obtained by use of the computer program described in Section 2.2, which performed isentropic expansion calculations up to the shocks and solved the oblique shock relations for the different deflection angles, with the constraint that the static pressures on both sides of the helium/air interface be equal. So that conditions downstream of the air shock be representative of a high-pressure ablation jet, it was desired that the pressure upstream of the air shock be approximately 5 atm. Parameters used as input to the program were the arc-heater reservoir conditions, the air nozzle Mach number, the helium nozzle reservoir conditions, and the impingement angle between the two jets. Results of these calculations are given in Fig. 25. Note that the static pressure downstream of the air shock is 15.95 atm for the 20-deg deflection case. This impingement angle of 20 deg was selected for further detailed analyses of the configuration, mainly because of anticipated design problems with use of smaller angles.

4.1.2 Light-Gas Acceleration Nozzle Analysis

Flow in the helium nozzle was analyzed with the one-dimensional particle acceleration program described in Section 2.1. The throat

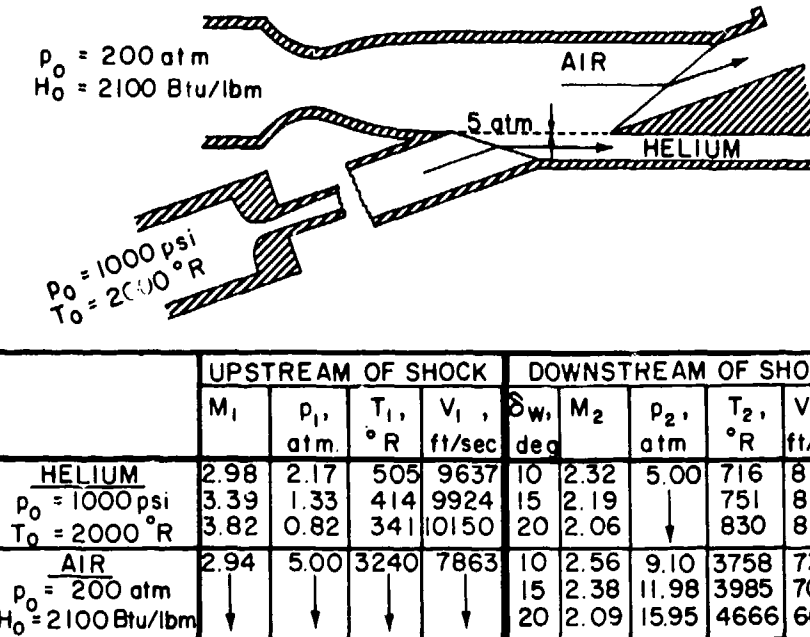


Figure 25. Results of flow-field calculations for proposed ablation/erosion nozzle.

diameter was assumed to be 0.119 in. The required static pressure in the helium flow upstream of the shock is 0.82 atm for the 20-deg deflection case (Fig. 25), and this determined the length of the helium nozzle to be 18.2 in. The results of the boundary-layer calculations indicate a merging of the boundary layer several inches upstream of the 18.2-in. length. In view of the uncertainty of the effect of the boundary layer merging on the particle acceleration, operation of the nozzle will be attempted in this configuration. However, if merging creates a serious problem in practice, it may be necessary to increase the nozzle divergence in this region. Calculations were made for MgO particles having various diameters between 10 and 1,000 μ , and the final particle velocities were found to range from 8,000 to 1,700 ft/sec. The final gas velocity was 10,150 ft/sec.

4.1.3 Particle Trajectory Calculations

The two-dimensional trajectories of particles crossing the four flow field regions of Fig. 25 were calculated with the program described in Section 2.2. Calculations were made for the 20-deg impingement case and with MgO particle diameters from 10 to 1,000 μ . As a conservative measure to allow for possible boundary-layer merging, the initial particle velocities for the trajectory calculations were assumed to be those at the nozzle point rather than at the end of the nozzle. It was found that there

was a strong tendency for the trajectories downstream of the helium shock to converge to a single trajectory. This results from the fact that the initial velocities developed in the acceleration nozzle vary inversely with the particle size or mass. In Fig. 26, the trajectories of all particles in the range from 50 to 1,000 μ are shown as a single curve. The 10- μ particles, however, showed substantially greater deviation from a straight line and are represented by a separate curve. A summary of particle trajectory parameters is given in Table 4 for the five locations indicated in Fig. 26.

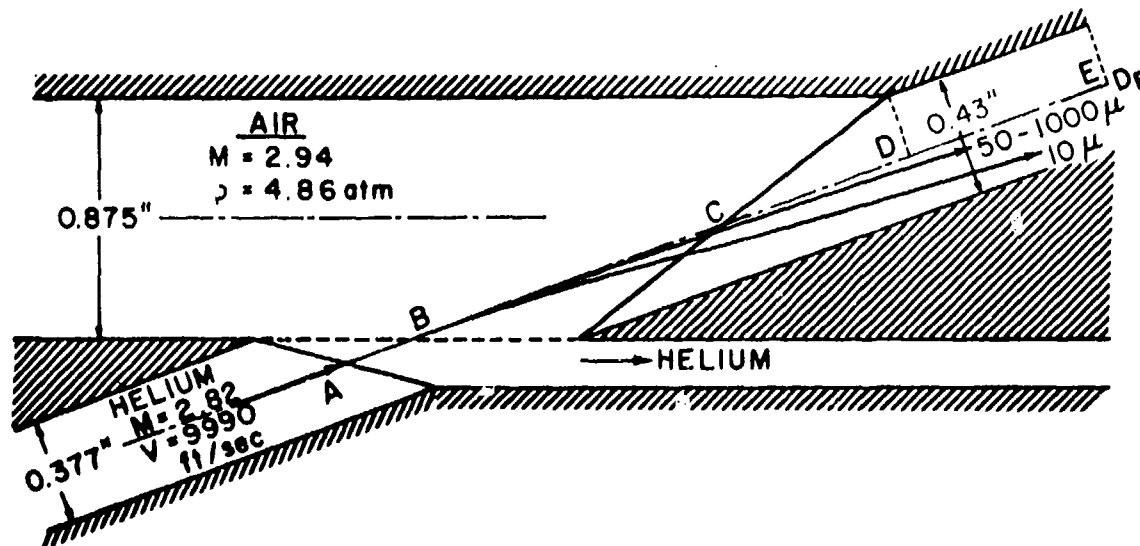


Figure 26. Particle trajectories calculated in ablation/erosion nozzle.

Table 4. Characteristics of Trajectories in Ablation/Erosion Nozzle

LOCATION	NORMAL DEF., inches			$\Delta\theta$, degrees			PARTICLE VELOCITY ft/sec		
	$D_p = 10 \mu$	100μ	1000μ	10μ	100μ	1000μ	10μ	100μ	1000μ
A-HELIUM SHOCK	0	0	0	0	0	0	8028	4390	1700
B-He/AIR BOUNDARY	.0014	.0004	.0005	0.62	0.16	0.21	8030	4405	1713
C-AIR SHOCK	.0511	.0158	.0192	4.57	1.34	1.61	7918	4510	1808
D-2.14" FROM He SHOCK	1.34	.0339	.0406	3.74	1.31	1.52	7604	4547	1890
E-2.86" FROM He SHOCK	1.524	.0505	.0575	3.22	1.28	1.45	7427	4578	1953

It is evident that particles having diameters from 50 to 1,000 μ deflect 0.05 to 0.06 in. normal to the initial direction and the velocity vector is turned by only 1.3 to 1.5 deg. These trajectories are essentially straight lines. The nozzle could be used as shown in Fig. 26 or the geometry could be tailored to the trajectories by a small rotation of the upper surface of the skimmer. The linear and angular deflections of the 10- μ particles are approximately three times larger than for the larger particles. Since the proposed facility concept will operate with 100- μ particles, this is not a handicap to the design.

4.1.4 Skimmer Heat Transfer

The skimmer section will no doubt present a difficult design problem because of the high heat-transfer rates. Calculations of the turbulent heating rates on the air side of the skimmer give values approaching 10,000 Btu/ft²-sec near the tip, but average values over the first inch are only 5,700 Btu/ft²-sec. The average heat load could easily be absorbed by internal water cooling; however, the sharp tip of the skimmer may have to be rounded slightly to reduce the peak heating locally. There may also be some slight relief as a result of laminar heat transfer near the tip.

4.1.5 Use of Hydrogen as Accelerator Gas

The performance of the acceleration nozzle could, of course, be increased by increasing the reservoir temperature of the helium. Ultimate maximum performance of the nozzle could be obtained by the use of hydrogen, since it has twice the specific heat of helium. Preliminary calculations were made for hydrogen in the present nozzle, and for the same light gas reservoir conditions of 1,000 psi and 2,000°R, velocities of 100- μ MgO particles were indicated to be 7,170 ft/sec, compared with 4,390 ft/sec in the helium nozzle. However, the boundary-layer calculation indicates that a substantially earlier merging and attainment of the hydrogen performance would be contingent upon avoiding any problems associated with boundary layer merging. In addition, the use of hydrogen would present many safety problems and hazards which would require thorough investigation.

4.2 DETAIL DESIGN OF A FIRST-GENERATION ABLATION/EROSION NOZZLE

For the purpose of proof-testing a first generation ablation/erosion nozzle, it was decided to relax the arc-heater operating conditions to 150 atm in order to avoid troublesome operational problems with the arc heater.

A design stagnation enthalpy of 2,200 Btu/lbm was chosen for this pressure level. It was felt that these conditions will provide a reasonable ablation environment in which to assess performance of the nozzle. Reservoir conditions for the light-gas acceleration nozzle were chosen to be 1,000 psi and 1,750°R, using helium. This also represents a small relaxation in operating conditions from those used in the analytical feasibility study (Section 4.1). Velocities of 100- μ MgO particles should still be in the vicinity of 4,000 ft/sec, which is considered adequate for the proof test.

The design Mach number for the arc-heater nozzle was determined by an isentropic expansion from the arc-heater conditions to the desired 5-atm pressure at the helium/air interface. The acceleration nozzle Mach number was also determined by the 5-atm matching condition and the helium reservoir conditions, using the oblique shock relation. The Mach numbers, pressures, temperatures, and calculated particle velocities for 100- μ MgO are given in Table 5 for the design version ablation/erosion nozzle.

Table 5. Design Conditions for First-Generation Ablation/Erosion Nozzle, Hot-Flow and Cold-Flow Versions

	GAS	UPSTREAM OF SHOCK				DOWNSTREAM OF SHOCK					
		M ₁	P ₁ atm	T ₁ °R	V ₁ ft/sec	M ₂	P ₂ atm	T ₂ °R	V ₂ ft/sec	P _{2'} atm	V _{p100u} ft/sec
HOT FLOW VERSION	HELIUM $P_0 = 1000 \text{ psi}$ $T_0 = 1750^\circ\text{R}$	3.819	0.818	299	9494	2.058	5.0	755	8139	-	4491
	AIR $P_0 = 150 \text{ atm}$ $H_0 = 2200 \text{ Btu/lbm}$	2.731	5.0	3647	7790	1.923	16.0	4970	6300	78.5	4491
COLD FLOW VERSION	HELIUM $P_0 = 735 \text{ psi}$ $T_0 = 500^\circ\text{R}$	3.426	0.943	101	4973	1.897	5.0	227	4115		2997
	AIR $P_0 = 735 \text{ psi}$ $T_0 = 500^\circ\text{R}$	2.157	5.0	259	1702	1.365	14.6	364	1277	42.8	2997

4.2.1 Arc-Heater Nozzle Design

A basic decision was made to use two-dimensional nozzles in order to simplify the geometry of the intersection of the two flows. The exit of the arc-heater nozzle was chosen to be 0.70 in. square. A nozzle expanding only in one direction was selected, giving a throat cross section of 0.189 by 0.70 in. for the design Mach number of 2.731. The nozzle

contour was obtained by a two-dimensional method-of-characteristics program. A boundary-layer correction was calculated but was deemed to be too small to include in the final contour. This nozzle will be cooled with 500-psi demineralized water flowing through back-side passages (Fig. 27).

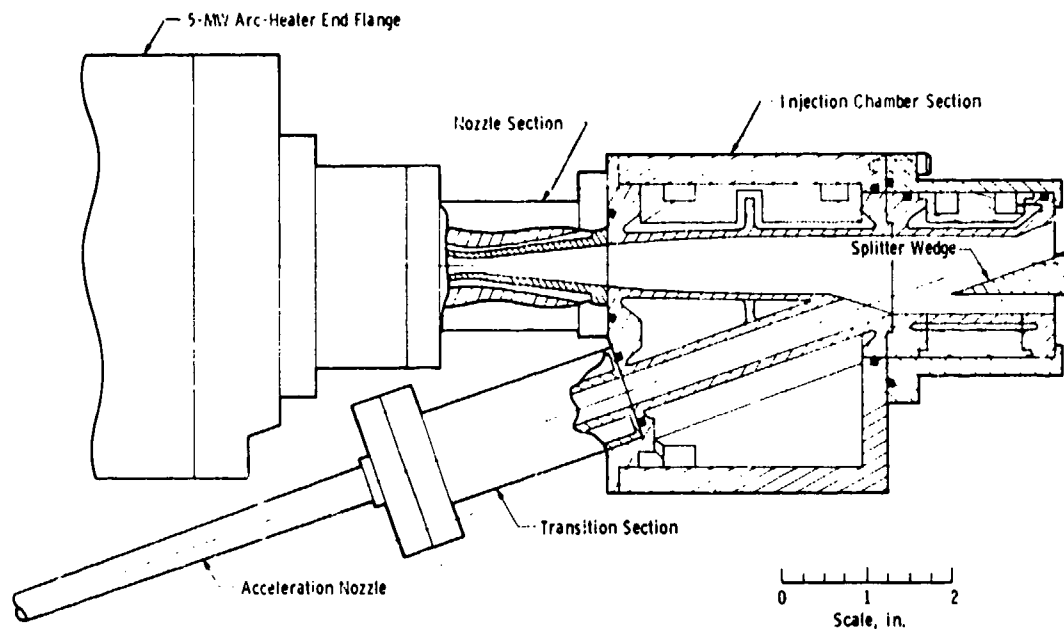


Figure 27. Cross section of ablation/erosion nozzle, hot-flow version.

4.2.2 Helium Particle Acceleration Nozzle

The gas heater, stilling chamber, particle injection system, and particle acceleration nozzle described in Section 3.1.2.1 were incorporated into the design of the first-generation ablation/erosion nozzle, with the exception that the nozzle was cut off at the length necessary to obtain the correct static pressure. This length was determined by calculations with the one-dimensional program described previously.

A round-to-square transition section (0.364-in. -diam to 0.364-in. -square) was designed to be located between the acceleration nozzle and the injection assembly. Since this nozzle will be operated with no cooling, provision must be made for thermal expansion. The end of the acceleration nozzle is allowed to slide inside the transition section, and while this will create some disturbances in the flow, it is preferable to attempting to cool the entire nozzle.

4.2.3 Injection Chamber or Assembly

The dimensions of the injection chamber are determined by the exit dimensions of the arc-heater nozzle (0.7 in. square) and the helium acceleration nozzle (0.412 in. square). The mixing region between the two gases was originally assumed to be thin and was neglected. This assumption is currently being reassessed, based on results with the cold-flow nozzle test described in Section 5.0. To allow for uncertainty of the mixing layer thickness and to permit fabrication to proceed, the injection chamber was split into two sections (Fig. 27). This feature also has the advantage of providing an easily replaceable piece in the region which is most likely to receive particle erosion damage.

Design of the splitter wedge to be located in the downstream section of the chamber has not been completed. The heat-transfer conditions noted in Section 4.1.3 suggest the use of either a water-cooled copper wedge or an uncooled wedge made of some high temperature ablation material. In either case, it will be impossible to preserve a perfectly sharp tip on the skimmer and an adjustment in position will be required to allow for shock detachment at the nose of the skimmer.

5.0 DESIGN AND TESTING OF COLD-FLOW ABLATION/EROSION NOZZLE

It was decided early in the study of the ablation/erosion nozzle concept that it would be desirable to design, construct, and operate a cold-flow version of this nozzle prior to final fabrication of the hot-flow version. This would permit identification of operational problems in time to allow design modification of the hot nozzle, serve as a check on the design calculation methods, and, incidentally, demonstrate experimentally that particle transfer across the mixing layer was possible.

5.1 DESIGN CONSIDERATIONS

The requirement of 5-atm static pressure at the mixing layer between the two flows was retained in the cold-flow version. The throat for the nozzle simulating the arc-heated flow was chosen to have essentially the same area as the standard 0.375-in.-diam nozzles used in most AEDC arc heaters, with reservoir conditions of 735 psi and 500°R to give an air mass flow of 2 lb/sec. The design Mach number of 2.157 for this nozzle was determined by the ratio of static to reservoir pressure, and this Mach determined the oblique shock angle on the splitter wedge for

the 20-deg deflection angle. The particle acceleration nozzle and particle injection system were considered identical to the hot nozzle version. The design conditions for the cold-flow version of the ablation/erosion nozzle are given in Table 5.

5.2 EXPERIMENTAL APPARATUS

The components of the cold-flow nozzle are the cold-flow air nozzle, the helium acceleration nozzle, and the particle injection section or chamber (Fig. 28). Also used in cold-flow testing are a laser shadowgraph system and the usual instrumentation systems. A photograph of the assembled system is shown in Fig. 29.

5.2.1 Cold-Flow Air Nozzle

The exit of the cold-flow air nozzle was 0.5-in. square, and the throat dimensions were 0.235 in. wide and 0.50 in. high. The contour of this nozzle was obtained by a two-dimensional method-of-characteristics program with a boundary-layer correction added. This nozzle was fabricated from 2024-T4 aluminum, selected for ease of fabrication. It was

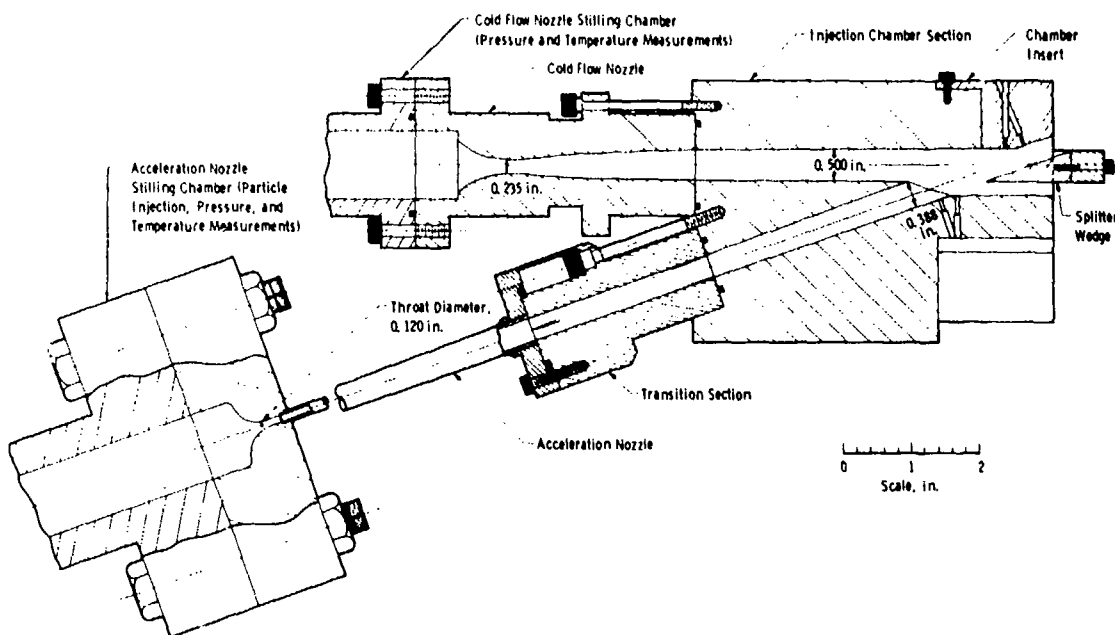


Figure 28. Cross section of ablation/erosion nozzle, cold flow version.

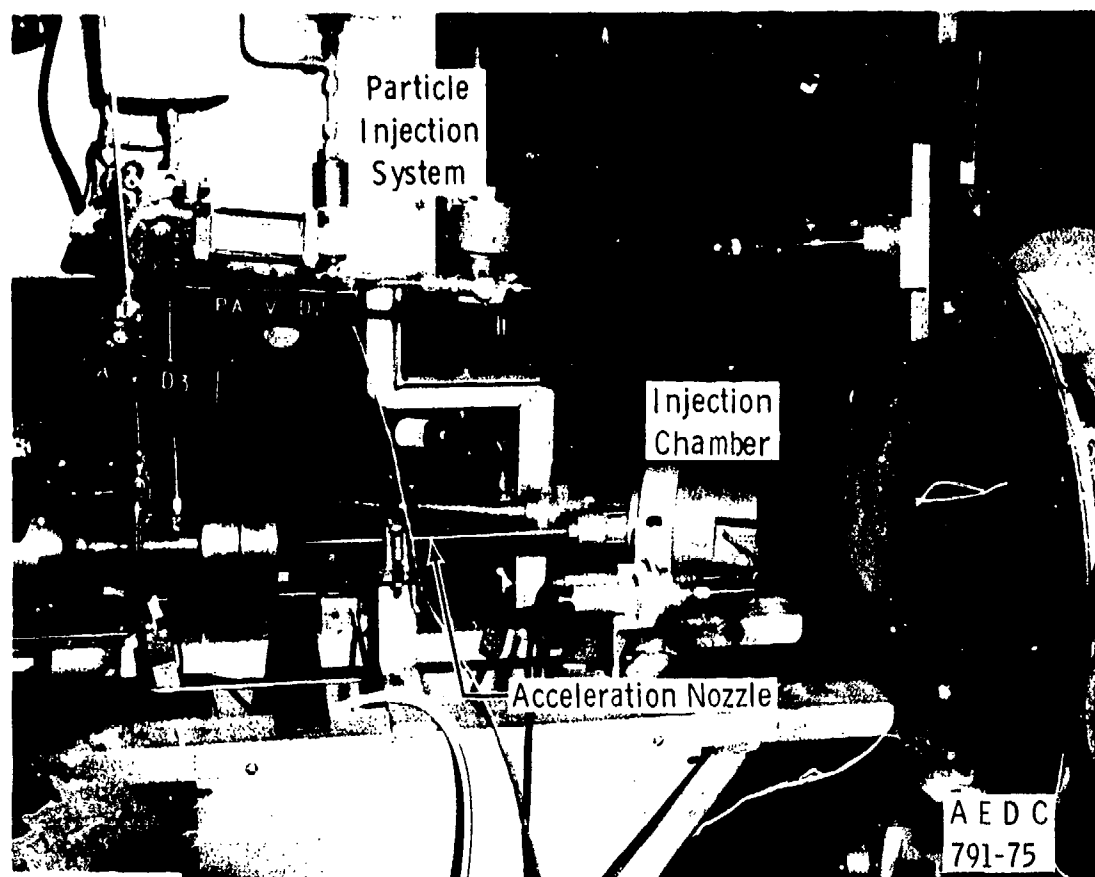


Figure 29. Photograph of cold-flow ablation/erosion nozzle apparatus.

supplied by a high-pressure air line or by a gaseous-nitrogen supply line. Either system was capable of passing the 2-lb/sec mass flow required and the stagnation pressures were controllable from atmospheric to over 750 psi. The design Mach number of 2.157 is low enough that liquefaction was not a concern; however, condensation of water vapor in the air supply was found to be a problem.

5.2.2 Acceleration Nozzle and Transition

It was necessary to shorten the acceleration nozzle to provide the correct static pressure (0.94 atm) at the correct exit Mach number of 3.43. As in the hot-flow version, a round-to-square transition section fabricated from 6061-T6 aluminum was provided between the end of the acceleration nozzle and the mixing chamber or particle injection section.

Helium supply for this nozzle was provided by a 2,200-psi helium trailer. Some testing was also done with both the air and nitrogen supply referred to above.

5.2.3 Particle Injection Chamber

The size of the section in which the particles were injected into the airflow was determined by the exit dimensions of the cold air nozzle and the helium acceleration nozzle (0.50 and 0.388 in. square, respectively) and by the requirement for a 20-deg impingement angle between the two flows. Oblique shock calculations yield a cold airflow exit height of 0.321 in. The mismatch between this dimension and the exit dimension of the acceleration nozzle will require that some particles will impinge on the upper wall of the injection chamber. Accordingly, a removable insert was fabricated which allows for easy replacement of this area (Fig. 28).

Static pressure orifices were provided in the injection chamber to allow measurement of pressure upstream and downstream of the helium and air shock waves. In addition, the sidewalls of the injection chamber were fabricated of removable sections of schlieren-quality glass to allow shadowgraph studies of the flow field.

The stainless steel splitter wedge was also located in the injection chamber. Provision was made for varying the angle of attack and axial position of the wedge to permit study of the effect of wedge orientation on the injection chamber flow field. The wedge position could not be varied during a run; however, rapid changes are possible between runs.

5.2.4 Laser Shadowgraph System

Most of the equipment used in the attempt to obtain particle field holograms was readily adapted to a shadowgraph system. For rapid viewing of test results, a Spectra-Physics Model 135-5 5-mw helium-neon laser was used with high-speed Polaroid® black and white film. If these shadowgrams were considered useful, an Apollo ruby laser was used to obtain a higher-quality permanent record in which considerably more flow details are visible.

5.3 EXPERIMENTAL RESULTS

A limited number of shakedown runs was made with the windows and skimmer wedge removed from the injection chamber assembly. Both helium and air were used in the particle acceleration nozzle for

these runs. The initial runs were made with helium and resulted in a slight erosion on the removable insert on the top wall of the particle injection chamber, apparently the result of residual dust left in the stilling chamber after previous runs of the particle acceleration nozzle. When the particle acceleration nozzle was operated with air, however, the erosion on the insert was much greater, and it was concluded that this was the result of ice particles formed in the expansion of moist air. The eroded area matched almost exactly the height of the particle acceleration nozzle, thus giving inadvertent proof of particle transfer across the mixing layer in essentially linear trajectories. In subsequent operations, the use of moist air in the light-gas acceleration nozzle was avoided.

For the next series of tests, the flow was properly confined to the injection chamber by installation of the windows, and runs were made without the skimmer wedge to investigate the nature of the mixing layer when undisturbed by the presence of the wedge. A shadowgram of a typical test condition is given in Fig. 30. The mixing region is clearly seen and is observed to propagate into the airflow region at a constant rate. Little penetration into the helium flow from the acceleration nozzle is noted. Some evidence of separation is observed in the airflow upstream of the junction with the helium flow and a weak oblique shock results. The



Figure 30. Shadowgraph of flow in cold-flow nozzle, no skimmers.

mixing region has a considerable thickness even at the far upstream end of the region. It was also observed during these tests that the pressure measured at the upstream pressure tap in the acceleration nozzle did not match the calculated value and, in fact, closely matched the value calculated for the region downstream of the shock. This indicated that the oblique shock in the helium flow was displaced upstream of its calculated position.

The skirmmer wedge was next installed at its intended location, and the cold-flow ablation/erosion nozzle was operated with nitrogen and helium at near design conditions. A shadowgram of the flow with the wedge in this position is given in Fig. 31. A prominent mixing layer is noted, with a

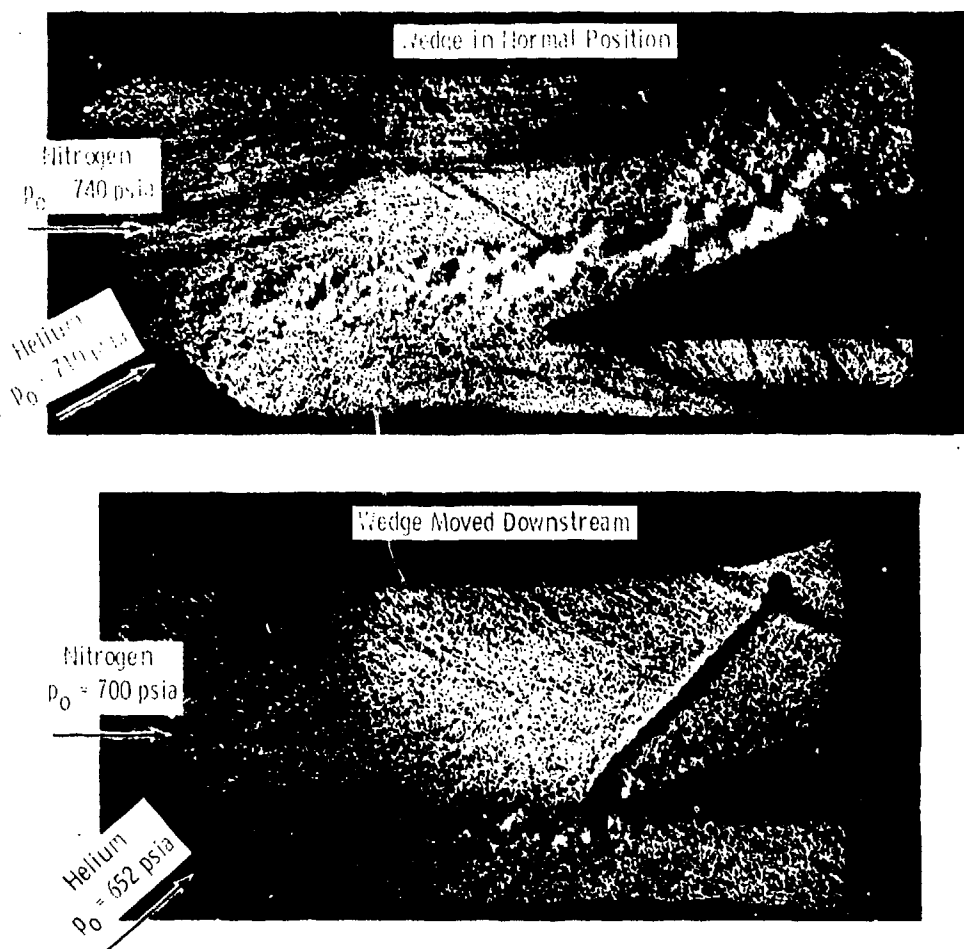


Figure 31. Shadowgraphs of flow in cold-flow nozzle, with wedge skimmer, normal wedge position, and adjusted wedge position.

relatively strong oblique shock originating at the beginning of the mixing layer. The mixing layer is deflected into the main airflow stream, which apparently narrows the flow channel and causes subsonic flow in this region. It was assumed that proper adjustment of the operating pressures of the two nozzles would restore the intended flow configuration.

The airflow nozzle stagnation pressure was held near the design condition, and the helium nozzle stagnation pressure was lowered to 400 psi. Although the upstream static pressure in the airflow did not indicate that supersonic flow had been established, examination of shadowgrams revealed a thinner mixing layer and a more regular shock structure. The mixing layer, however, was still deflected above the wedge. Analysis of both the pressure measurements and the shadowgrams suggested that the wedge was acting like a two-dimensional blockage in a supersonic wind tunnel. It was decided to move the wedge downstream and tilt it upward until the area required to allow supersonic flow above the wedge was achieved. In addition, some material was removed from the lower surface of the wedge in an effort to improve the flow in the helium leg downstream of the wedge tip. A shadowgram of the flow made after these changes shows considerable improvement in the flow field (Fig. 31). The mixing region is once again the thickness attained during the tests without the wedge, and it now intersects the wedge at the proper location. The shock structure in the airflow region of the injection chamber is close to design, although it is located too far downstream to intersect the corner of the insert on the upper surface. The Mach number calculated from the 20-deg deflection angle and the shock angle on the wedge is 2.048, compared with the design value of 2.157. This reduction in Mach number was presumed to be the result of blockage by the mixing layer. An effort was made to calculate this blockage effect with an existing mixing layer program, and a Mach number of 2.05 was the result, very close to the measured value. (Note that this reduction in Mach number is not the result of boundary-layer displacement in the air nozzle, since a boundary-layer correction was added to the inviscid nozzle contour.)

The static pressures measured at the "upstream" orifice in the helium flow continued to indicate that the shock wave was upstream of this location. If it is assumed that the shock position is just upstream of this orifice, it is possible to calculate new values of Mach number and static pressure in the helium flow from the oblique shock equations. These values match, within a few percent, values obtained during operation of the light-gas acceleration nozzle alone. This indicates that the transition section is functioning properly and that the oblique shock is at an angle greater than design for some reason.

To benefit from the experience gained in operation of the cold-wall version of the ablation/erosion nozzle, the design of the hot-flow version will be slightly modified to allow for the greater than expected blockage of the mixing layer. The hot-flow version, from the beginning, has had the requirement that the dimensions of the final ablation/erosion jet be equal to the exit of the light-gas acceleration nozzle, to minimize particle erosion within the nozzle.

6.0 CONCLUSIONS

Results of a test to analyze, design, and test the components of a combined ablation/erosion nozzle may be summarized as follows:

1. An analytical study was made to determine the possibility of attaining a combined ablation and erosion test environment in a facility which has operating times measured in seconds.
2. Computer programs were developed and/or extended for analysis of one-dimensional particle/gas flows with thick boundary layers and for analysis of two-dimensional particle trajectories in various gas flow fields. An empirical particle drag coefficient relation was developed based on most recent test data.
3. It was determined that direct drag-acceleration of $100\text{-}\mu$ -diam particles in typical low Mach number nozzles used in arc-heated ablation facilities was relatively ineffective. Such particles can be accelerated to hypervelocities in a long, slowly diverging nozzle in which length of exposure to high drag force is maximized.
4. By adopting the concept of acceleration of particles in a separate light-gas acceleration nozzle, followed by injection into an ablation jet by inertial transfer across a mixing layer between the two jets, detailed analysis indicates an erosion capability can be added to a state-of-the-art ablation jet.
5. A detail design was completed for a facility based on this concept, and a cold-flow version was built and operated to obtain operating experience with the new configuration. Particle velocities which were measured in the acceleration nozzle agreed well with the predictions of the one-dimensional

program. Aerodynamic calibration of the combined flow indicated that the displacement thickness of the mixing layer was substantial and should be allowed for in final design.

REFFRENCE

1. Johnson, Elmer G., MacDermott, W. N., and Kessel, P. A. "Prospects for an Ablation/Erosion Facility Employing the RHEA Concept." AIAA Paper No. 74-605, AIAA 8th Aerodynamic Testing Conference, Bethesda, Maryland, July 8-10, 1974.
2. Norman, Wendell and Siler, Leo G. "Experiments in a Shock Tunnel Augmented by a Magnetohydrodynamic Nozzle Accelerator." AEDC-TR-68-232 (AD844665), December 1968.
3. Ranz, W. E. and Marshall, W. R. "Evaporation from Drops, Parts I and II." Chemical Engineering Progress, Vol 48, March and April 1952, pp. 141-146, 173-180.
4. Crowe, C. T. "Drag Coefficient of Particles in a Rocket Nozzle." AIAA Journal, Vol. 5, May 1967, pp. 1021-1022.
5. Bailey, A. B. and Hiatt, J. "Free Flight Measurements of Sphere Drag at Subsonic, Transonic, Supersonic, and Hypersonic Speeds for Continuum, Transition, and Near-Free-Molecular Flow Conditions." AEDC-TR-70-291 (AD721208), March 1971.
6. Bailey, A. B. "Sphere Drag Coefficient for Subsonic Speeds in Continuum and Free-Molecular Flows." Journal of Fluid Mechanics, Vol. 65, No. 2, 1974, pp. 401-410.
7. Crowe, C. T., Babcock, W. R., and Willoughby, P. G. "Drag Coefficient for Particles in Rarefied Low Mach Number Flows." Paper 3-3, International Symposium on Two-Phase Systems, Technion City, Israel, 1971.
8. Korkan, K. D., Petrie, S. L., and Bodonyi, R. J. "Particle Concentration in High Mach Number Two-Phase Flows." ARL TR-74-0102, July 1974.

NOMENCLATURE

A	Flow area
A_p	Cross-sectional area of particle
$a_0, a_1, a_2,$ $b_0, b_1, b_2,$ $c_0, c_1, c_2,$ d_0, d_1, d_2	Coefficients in drag coefficient correlation, Eq. (2) and Table 2
C_D	Particle drag coefficient
C_f	Skin friction coefficient
C_h	Stanton number
C_p	Specific heat
C_1, C_2, C_3	Constants in Eq. (5) for skin friction
D	Diameter
H_o	Total enthalpy based on energy balance
h	Static enthalpy
M	Mach number of flow or relative flow
m_p	Mass of particle
Nu	Nusselt number
P_o	Impact pressure
Pr	Prandtl number
p	Static pressure of gas
\dot{Q}_p	Heat flow to particle
Re	Reynolds number

S_p	Particle surface area
T	Temperature
V	Velocity
v	Volume of particle
x	Streamwise coordinate
α	Angle of attack or angle of Prandtl-Meyer expansion ray
γ	Specific heat ratio
δ	Total thickness of boundary layer
δ^*	Displacement thickness of boundary layer
θ	Momentum thickness of boundary layer or angle of velocity vector
μ	Viscosity
ρ	Density
$\overline{()}$	Barred quantity is an average value across the flow
$()$	Unbarred quantity is value in the isentropic core of the flow
$(\vec{ })$	Vector quantity

SUBSCRIPTS

calc	Calculated value
inc	Incompressible value
meas	Measured value
o	Reservoir condition

p Particle
t Total condition
w Wall condition